JCI insight

HPV8-induced STAT3 activation led keratinocyte stem cell expansion in human actinic keratoses

Huw J. Morgan, … , Marisa Gariglio, Girish K. Patel

JCI Insight. 2024. https://doi.org/10.1172/jci.insight.177898.

Research In-Press Preview Cell biology Stem cells

Graphical abstract

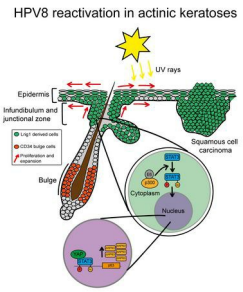

HPV8-induced STAT3 activation led keratinocyte stem cell expansion in human actinic keratoses

Huw J Morgan,*[1] Carlotta Olivero,*[1] Boris Y Shorning,[1] Alex Gibbs,[1] Alexandra L Phillips,[1] Lokapriya Ananthan,[1] Annabelle Xiao Hui Lim,[1] Licia Martuscelli,[2] Cinzia Borgogna,[2] Marco De Andrea,[3,4] Martin Hufbauer,[5] Richard Goodwin,[6] Baki Akgül,[5] Marisa Gariglio,[2] Girish K Patel[1]

1 European Cancer Stem Cell Research Institute, School of Biosciences, Cardiff University, Maindy Road, Cardiff, UK

2 University of Piemonte Orientale, Dept. of Translational Medicine, Via Solaroli, 17 - 28100 Novara, Italy

3 Viral Pathogenesis Unit, Department of Public Health and Pediatric Sciences, University of Turin, Medical School, 10126 Turin, Italy

4 Intrinsic Immunity Unit, CAAD - Center for Translational Research on Autoimmune and Allergic Disease, University of Eastern Piedmont, 28100 Novara, Italy

5 Institute of Virology, University of Cologne, Medical Faculty and University Hospital Cologne, Cologne, Germany

6 Department of Dermatology, Aneurin Bevan University Health Board, Royal Gwent Hospital, Newport, UK

Correspondence: Girish K Patel, European Cancer Stem Cell Research Institute, Cardiff University, CF24 4HQ, Tel: (+44) 02920 88520, Email: PatelGK@Cardiff.ac.uk

* Authors contributed equally to this work

Conflict-of-interest statement: The authors have declared that no conflict of interest exists.

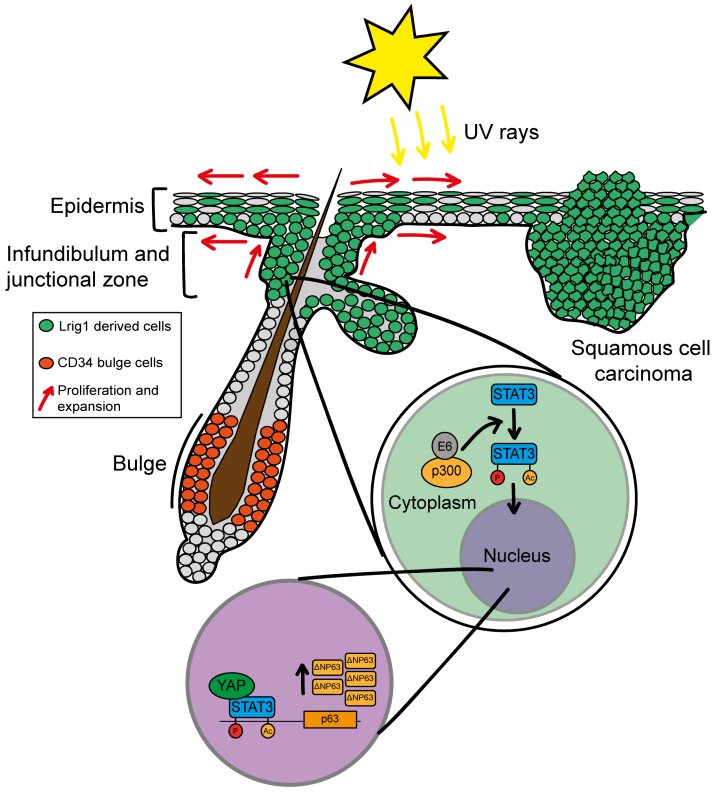
HPV8 reactivation in actinic keratoses
UV rays
Epidermis
Infundibulum and junctional zone
Lrig1 derived cells
CD34 bulge cells
Proliferation and expansion
Bulge
Squamous cell carcinoma
STAT3
E6
p300
STAT3
P
Ac
Cytoplasm
Nucleus
YAP
STAT3
P
Ac
ΔNP63
ΔNP63
ΔNP63
ΔNP63
p63

Abstract

Despite epidermal turnover, the skin is host to a complex array of microbes including viruses, such as the human papillomavirus (HPV), which must infect and manipulate skin keratinocyte stem cells (KSC) to survive. This crosstalk between the virome and KSC populations remains largely unknown. Here, we investigated the effect of HPV8 on KSCs using various mouse models. We observed that the HPV8 early region gene E6 specifically caused Lrig1$^+$ hair follicle junctional zone KSC proliferation and expansion, which would facilitate viral transmission. Within Lrig1$^+$ KSCs specifically, HPV8 E6 bound intracellular p300 to phosphorylate the STAT3 transcriptional regulatory node. This induces ΔNp63 expression, resulting in KSC expansion into the overlying epidermis. HPV8 was associated with 70% of human actinic keratoses (AK). Together these results define the “hit and run” mechanism for HPV8 in human actinic keratosis as an expansion of KSCs, which lacks melanosome protection and is thus susceptible to sun-light-induced malignant transformation.

Introduction

Human skin hosts a microbiota that has maintained symbiosis through evolution. Integral to this environmental interface is a large and diverse array of viruses, the virome, which is capable of manipulating host cellular processes to reside as symbionts (1–3). As obligate intracellular parasites, notably *Papillomaviridae* have to infect long-lived cells such as skin keratinocyte stem cells (KSC) to withstand constant epidermal turnover (4). Among the various skin KSC populations, the hair follicle (HF) KSCs have been implicated as host cells for *Beta-papillomaviruses* (5–7). Recently, HF KSCs have been identified as important regulators in the crosstalk between the bacterial microbiome and the immune system(8–11). The virome is unaffected by antibiotics, yet similar to the bacterial microbiome, expansion, and diversification are observed with impaired immunity. Relative to healthy individuals, subtle shifts in immune function such as in epidermodysplasia verruciformis (EV) or dedicator of cytokinesis 8 (DOCK8) deficiency, directly alter the virome leading to increased diversity and expanded representation of skin tropic β and γ human papillomavirus (HPV) types, which in turn increase the risk of skin cancer (12–15). Similarly, alterations in virome have been observed among solid organ transplant recipients on immunosuppression, who exhibit a 60-250-fold increased risk of skin cancer (16–22). As such, there is a clinical imperative to elucidate the crosstalk between HPV and host KSCs.

The *Papillomaviridae*, HPV family, are small (7-8 kb) non-enveloped DNA viruses that undergo episomal replication within differentiating keratinocytes. HPV contains three distinct coding regions: (1) an upstream regulatory region, (2) an early region with typically up to six open reading frames (E1, E2, E4, E5, E6 and E7), and (3) a late region encoding capsid proteins L1 and L2 (23, 24). Tissue tropism is determined by the L1 protein, with negatively charged L1 protein of β and γ HPV types selectively targeting human non-mucosal skin, while the positively charged L1 protein on α HPV types result in mucosal infection (24, 25). Micro-abrasion facilitates viral entry into basal keratinocytes, and therein KSCs, in order to

establish long-term infection, wherein E1 and E2 proteins support replication of the viral genome at a low copy number. It is only when these infected basal cells differentiate, thus moving closer to the surface, that the viral load increases to support viral transmission (26).

In the majority, HPV infection is an asymptomatic infection that may result in transient warts or keratoses, countered by the immune response that blocks viral replication. However, persistent infection with high-risk HPV types, notably α HPV, is associated with cancer accounting for an estimated 600,000 cases per annum (27). In α HPV, viral integration into the host DNA is postulated to deregulate expression of E6 and E7 proteins leading to keratinocyte transformation, however, transformation can also occur without integration (28). In the complex structure of the skin with appendageal structures, high-risk β HPV (HPV5, 8, and 38) have been associated with pre-malignant skin changes, called actinic keratoses (AK), which in association with ultraviolet (UV) light exposure, risk transformation to cutaneous squamous cell carcinoma (cSCC) (16–18, 29–36). However, β HPV DNA integration is not observed, and the viral load in ensuing cSCC is low, leading authors to postulate a “hit and run” mechanism for transformation (30, 37).

Consistent with the potential oncogenic role of high-risk β HPV, FVBN transgenic mice expressing HPV8 early region genes under the control of the keratin 14 (Krt14) promoter (HPV8-CERtg) exhibit skin changes mirroring human AK and spontaneously develop cSCC, which occur with greater frequency after UV light exposure (38, 39). HPV8-CERtg mice crossed with Rag 2 deficient mice, to recreate the immunosuppressive tumor microenvironment similar to that observed in organ transplant recipients on immunosuppressants, demonstrated accentuated tumor growth (40). In addition, cSCC has also been observed in transgenic mice expressing individual HPV8 early region genes E2, E6 and E7 under the control of the Krt14 promoter (41–43). Recently we identified that the HF junctional zone KSC (herein denoted as JZSC) population, defined by the expression of leucine-rich repeats and immunoglobulin-like domains protein 1 (Lrig1) on the cell surface,

was selectively expanded in the HPV8-CERtg mice (38). In this manuscript, we elucidate the crosstalk between HPV8 and KSCs, redefining the basis for AK, and thus identify HPV8 to be a major risk factor for human cSCC.

Results

The HF contains multiple KSC populations that under homeostatic conditions maintain keratinocyte numbers during hair cycling, but also retain the capacity to regenerate the whole HF (Figure 1A). To determine how HPV8 selectively drives the proliferation and expansion of the Lrig1$^+$ JZSC population we utilized the HPV8-CERtg mouse model, wherein the Krt14 promoter regulates the expression of the HPV8 early region genes in basal cells of the entire epithelium (Supplemental Figure 1A). Immunofluorescent labeling of skin with antibodies binding to the basal keratin, Krt14 and the differentiation marker involucrin showed that the HPV8-CERtg compared to wild type (WT) had an expansion of the undifferentiated keratinocytes within the infundibulum and overlying epidermis, with a reduction in the involucrin:Krt14 ratio (Figure 1B). To confirm that Lrig1$^+$ JZSC proliferation led to expansion into the infundibulum and overlying epidermis, we crossed Lrig1CreER^{T2}:R26RConfetti and Krt15CrePGR:R26RConfetti mice with HPV8-CERtg mice (Figure 1C). The Confetti mouse contains a four-color cassette, which recombines within individual cells upon Cre activation to express one of four fluorescent proteins: green (GFP), red (RFP), yellow (YFP) or cyan (CFP) (44). In WT Lrig1CreER^{T2}:R26RConfetti and Krt15CrePGR:R26RConfetti mice, lineage-labeled progeny as expected remained compartmentalized to the infundibulum and sebaceous gland (Lrig1CreER^{T2}:R26RConfetti mice) or to the lower hair follicle and inner root sheath (Krt15CrePGR:R26RConfetti mice) (Figure 1D). Likewise Krt15CrePGR:R26RConfetti:HPV8-CERtg mice showed a similar distribution of labeled cells compared to their WT counterpart. However, Lrig1CreER^{T2}:R26RConfetti:HPV8-CERtg mice showed fluorescent clones extending into the infundibulum and perifollicular epidermis (Figure 1D). Thus, HPV8-induced selective proliferation of the Lrig1$^+$ JZSC population resulted in the expansion of this population into the infundibulum and perifollicular epidermis.

c-MYC transcriptional regulation distinguishes JZSC from HF bulge KSC during homeostasis

Lrig1$^+$ JZSCs are transcriptionally distinct from the lower HF bulge KSC populations, which are typically characterized by CD34 cell surface expression (38, 45, 46). To determine why HPV8 induced selective proliferation of the Lrig1$^+$ JZSCs, but not other KSCs, we undertook a transcriptomic analysis of these adjacent HF KSC populations defined by Lrig1 and CD34 expression in adult mice. Both Lrig1$^+$ and CD34$^+$ flow-sorted keratinocytes were isolated from dorsal back skin of individual mice, using established protocols, for pairwise comparison (Figure 1E). Illumina HiSeq4000 paired-end sequenced samples resulted in a total of 35,566,700 reads, of which 47% mapped to 54,658 murine genes (GRCm38). Principal-component analysis distinguished both genotype and KSC population transcriptomes (Figure 1F). Unsupervised hierarchical clustering of Log_2 transformed, median centred, average linkage by Pearson's correlation showed primary segregation of KSC populations with the influence of HPV8 as a secondary separation (Supplemental Figure 1B), suggesting that the regulatory signaling pathway networks between adjacent KSC populations are largely distinct and independent of the effects of HPV8 early region genes. Normalization of count data and DESeq2 pipeline analysis, identified 3029 differentially expressed genes (DEGs; $p < 0.05$) from Lrig1$^+$ vs CD34$^+$ flow-sorted keratinocytes in WT mice (Figure 1G and Supplemental Table 1). These DEGs were enriched for 330 genes that distinguish Lrig1$^+$ from CD34$^+$ KSC populations previously identified by microarray analysis (Supplemental Figure 1C)(46). Gene set enrichment analysis (GSEA)(47, 48) of the DEGs determined that the Lrig1$^+$ JZSCs were involved in upper-hair follicle and sebaceous gland differentiation (positive enrichment) and were distinct from the CD34$^+$ outer layers (negative enrichment) of the hair follicle bulge keratinocytes (Supplemental Figure 1D). GSEA identified c-Myc as the central regulating node that distinguished these two KSC populations, in WT and HPV8-CERtg, with Lrig1$^+$ JZSC flow-sorted keratinocytes showing a greater enrichment of the *c-Myc* signature when

compared with the CD34 population, consistent with the role of the JZSC in maintaining sebaceous gland sebocyte differentiation (Figure 1H). Thus, Lrig1 JZSCs under homeostatic conditions represent a distinct HF KSC population distinguished by activation of c-Myc.

Transcriptomic analysis of flow-sorted Lrig1$^+$ and CD34$^+$ KSC populations from adult HPV8-CERtg mice yielded 1427 DEGs, of which 46% overlapped with DEGs from similar analysis in WT mice (654 genes); consistent with the primary segregation found in our unsupervised hierarchical clustering. Bioinformatic analysis of HPV8-CERtg flow-sorted cells demonstrated findings that were similar to WT mice, but there was no further enrichment of *c-Myc* to account for increased proliferation from GSEA (Figure 1I), nor difference in transcript counts or *c-Myc* gene expression by qPCR (Figure 1J). Therefore, c-Myc activation differentiates Lrig1$^+$ and CD34$^+$ KSC populations in both WT and HPV8-CERtg HFs but was not responsible for the HPV8-induced proliferation of only the Lrig1$^+$ JZSC population.

STAT3 activation drives Lrig1 JZSC proliferation

While the bioinformatic analysis comparison of Lrig1$^+$ and CD34$^+$ HF KSC populations yielded a total of 3802 DEGs (Figure 1G), in contrast, there were a total of 276 DEGs ($p < 0.05$) from the analysis of HPV8-CERtg vs WT for the two HF KSC populations (Figure 2A). There were only two shared genes, β-1,4-galactosyltransferase 6 and olfactory receptor family 12 subfamily D member 3, suggesting that the transcriptional impact of HPV8 early region genes was unique to individual KSC populations even when closely situated, consistent with the observed increased proliferation of the Lrig1$^+$ JZSC but not the CD34 bulge KSC population.

We hypothesized that HPV8 must selectively activate a growth factor pathway(s) in the Lrig1$^+$ JZSCs but not the CD34 bulge KSC population for there to be selective proliferation. Therefore, we utilized Ingenuity Pathway Analysis canonical pathways comparative

213 software package (Qiagen), inputting all DEGs (adjusted $p < 0.05$, Supplemental Table 1)
214 from comparisons of HPV8 Lrig1 vs WT Lrig1 and HPV8 CD34 vs WT CD34. Only the
215 STAT3 signaling canonical pathway demonstrated activation and reached significance ($p <$
216 0.05) with differential expression in the Lrig1$^+$ HPV8 vs WT when compared to the CD34$^+$
217 HPV8 vs WT analyses (Supplemental Figure 1E). There was greater phosphorylated
218 STAT3 observed within hair follicle keratinocytes from HPV8-CERtg mouse skin
219 (Supplemental Figure 1F). Although glucocorticoid receptor, HIF1-α, and Hippo signaling
220 pathways also demonstrated differential expression, these did not reach significance.
221 GSEA of the STAT3 gene signature in the Lrig1 HPV8 vs Lrig1 WT mouse DEGs
222 demonstrated a normalized enrichment score of 1.1, whereas the CD34 HPV8 vs CD34 WT
223 comparison was only 0.6 (Figure 2B). Nuclear labeling of phosphorylated STAT3 was
224 evident within the hair follicle junctional zone, infundibulum and adjoining interfollicular
225 epidermis of HPV8tg skin, consistent with its role in driving Lrig1$^+$ JZSC proliferation and
226 expansion (Figure 2C). Western blot analysis of HPV8-CERtg and WT mouse back skin
227 keratinocytes identified similar levels of full-length and transcriptionally active STAT3α
228 (86kDa) as the predominant splice variant (Figure 2D). Consistent with activation of the
229 STAT3 pathway, HPV8-CERtg mouse skin nuclear fractions demonstrated 2.2-fold increase
230 in Tyr705 STAT3 phosphorylation (within the transactivation domain), but no change in
231 Ser727 STAT3 phosphorylation (within the COOH terminus) (Figure 2E). STAT3
232 downstream transcriptionally regulated genes were increased in expression by qPCR in
233 HPV8-CERtg Lrig1$^+$ JZSCs relative to the CD34+ bulge KSC population (Figure 2F).

234 To determine if the STAT3 regulatory node was essential for HPV8-induced Lrig1$^+$ JZSC
235 proliferation, we crossed HPV8-CERtg mice with Krt5Cre-Stat3$^{+/flox}$ mice to generate HPV8-
236 CER:STAT3$^{+/-}$tg mice, since STAT3 knockout is known to be embryologically lethal. We
237 have previously shown that HPV8-CER:STAT3$^{+/-}$tg mice had WT levels of Tyr705 STAT3
238 phosphorylation, and demonstrated a four-fold reduction in tumor formation (49). Confocal
239 laser scanning microscopy (CLSM) imaging using IMARIS™ 3D rendering software of

fluorescently labeled Lrig1$^+$ JZSCs in whole mount tail skin, showed no expansion in HPV8-CER:STAT3$^{+/-}$tg mice (Figure 2G). Consistent with the lack of KSC proliferation, *ΔNp63* expression levels in HPV8-CER:STAT3$^{+/-}$tg were comparable to those in WT skin (Figure 2H), specifically also in the Lrig1$^+$ flow-sorted cells (Figure 2I). Similarly, *ΔNp63* expression levels in the HPV8-CER:STAT3$^{+/-}$tg flow-sorted CD34$^+$ bulge KSCs remained unchanged (Supplemental Figure 1G). In summary, HPV8-induced Lrig1$^+$ JZSC proliferation was dependent upon STAT3 Tyr705 phosphorylation.

HPV8 E6-induced proliferation of Lrig1 JZSC

To determine which of the HPV8 early region protein(s) was responsible for STAT3 activation and therefore specific proliferation of the Lrig1$^+$ JZSC population, we compared the adult mouse skin HFs from WT, HPV8-CERtg and those expressing the individual early region genes: HPV8-E2tg, HPV8-E6tg and HPV8-E7tg (Figure 3A). Anagen HF lengths were similar between WT and the different mouse genotypes: WT (418.20±11.25μm), HPV8-CERtg (414.38±9.01μm), HPV8-E2tg (412.26±8.44μm), HPV8-E6tg (429.56±1.85μm) and HPV8-E7tg (430.43±13.31μm) (n>100 HFs per genotype in 3 mice per genotype) (Figure 3A). The expanded infundibulum area observed in the HPV8-CERtg (4.67±0.33 cells) compared to WT (2.33±0.33 cells) was also observed in the mice with individual early region genes E2 (3.13±0.29 cells) and E6 (4.56±0.29 cells), but not E7 (2.67±0.33 cells) (Figure 3A). Next, we fluorescently labeled Lrig1$^+$ JZSCs and used CLSM with IMARIS™ 3D rendering software of whole mount tail skin from mice expressing individual early region genes, HPV8-CERtg and WT (Figure 3B). Compared to WT (168.79±9.06 μm^3) the Lrig1$^+$ population volume in HPV8-CERtg (273.517±33.89 μm^3) and HPV8-E6tg alone (248.94±12.86 μm^3) were significantly larger (Figure 3B). In contrast, HPV8-E2tg (194.70±7.54 μm^3) and HPV8-E7tg (152.30±15.49 μm^3) demonstrated no significant increase in the Lrig1$^+$ JZSC population. The CD34$^+$ bulge KSC population was unchanged in the transgenic mice from that observed in WT mice (Supplemental Figure 2A). Proliferation, assessed by ki67 immunofluorescent labeling, was significantly greater in

the Lrig1$^+$ JZSC in HPV8-CERtg (15.00±4.51%) and HPV8-E6tg (14.50±2.56%) compared to WT (7.60±4.08%), whereas no increase was observed in: HPV8-E2tg (8.00±4.34%), and HPV8-E7tg (6.88±2.10%) (Figure 3B and Supplemental Figure 2B). As expected, there was no increase in proliferation within the CD34$^+$ HF bulge KSC population compartment in the transgenic mice compared to that in WT mice (Supplemental Figure 2A).

The Lrig1$^+$ JZSC population was quantified by flow cytometry in WT and transgenic mouse dorsal back skin keratinocytes labeled with Lrig1 and CD34. In contrast to the unchanged CD34$^+$ population, the Lrig1$^+$ population was greater in HPV8-CERtg (5.85±1.32%) and HPV8-E6tg (6.84±0.80%) transgenic mice compared to WT (3.05±0.65%), HPV8-E2tg (1.98±0.56%) and HPV8-E7tg (1.13±0.32%) (Figure 3C and Supplemental Figure 2B). Flow-sorted Lrig1$^+$ keratinocytes from transgenic and WT mice did not express *Cd34*, and similarly had low expression levels of other HF KSC markers *Lgr5* and *Lgr6* (Figure 3D). Consistent with KSC proliferation and enrichment, the Lrig1 population from HPV8-CERtg and HPV8-E6tg mice exhibited increased expression of *ΔNp63* relative to WT mice (Figure 3E) and reduced expression of differentiation-associated *Krt10* (Figure 3F). The reduction in *Krt10* expression was not observed in the CD34 population from the same mice when compared to WT (Supplemental Figure 2C). Flow-sorted Lrig1$^+$ keratinocytes demonstrated a four-fold increase in colony-forming efficiency (CFE) in the HPV8-E6tg Lrig1$^+$ population (0.24±0.11%) compared to WT (0.05±0.04%) (Figure 3G). Consistent with the E6-driven Lrig1$^+$ JZSC proliferation and expansion, the flow-sorted Lrig1$^+$ JZSCs retained elevated expression of *Sox9* and *c-Myc* compared to CD34$^+$ KSCs (Figure 3H and Supplemental Figure 2D). HPV8-E6tg mouse tissue sections had increased KSC proliferation-associated proteins YAP and P63 (Figure 3I). Thus, the HPV8 E6 alone was sufficient to cause HPV8-induced Lrig1$^+$ JZSC proliferation and expansion.

HPV8 E6 induces Lrig1$^+$ JZSC expansion into the overlying epidermis

HPV8-E6tg mouse skin nuclear fractions demonstrated 2.7-fold greater Tyr705 STAT3 phosphorylation, but no change in Ser727 STAT3 phosphorylation (Figure 4A). Next, we sought to determine whether HPV8 E6-driven Lrig1$^+$ JZSC proliferation was sufficient to cause expansion into the overlying epidermis by lineage tracing. We crossed Lrig1CreER^{T2}:R26RConfetti and Krt15CrePGR:R26RConfetti mice with HPV8-E6tg mice to generate Lrig1CreER^{T2}:R26RConfetti:HPV8-E6tg and Krt15CrePGR:R26RConfetti:HPV8-E6tg mice, wherein recombination occurred in nearly all cells (98%; data not shown). As before, Lrig1CreER^{T2}:R26RConfetti:HPV8-E6tg demonstrated epidermal fluorescence; consistent with Lrig1$^+$ JZSC proliferation and expansion into the overlying epidermis (Figure 4B). Confetti labeled cells could be identified by flow-cytometry in the GFP channel using the 488nm laser, enabling us to simultaneously identify Lrig1$^+$ cells by antibody labeling, such that we could isolate flow-sorted Lrig1$^+$ confetti$^+$ and their Lrig1$^-$ confetti$^+$ progeny from Lrig1CreER^{T2}:R26RConfetti:WT and Lrig1CreER^{T2}:R26RConfetti:HPV8-E6tg (Figure 4C). As expected there were more Lrig1$^-$ confetti$^+$ progeny in the Lrig1CreER^{T2}:R26RConfetti:HPV8-E6tg compared to Lrig1CreER^{T2}:R26RConfetti:WT. WB analysis of nuclear fractions demonstrated 2-fold greater Tyr705 STAT3 phosphorylation in Lrig1$^+$ confetti$^+$ and Lrig1$^-$ confetti$^+$ from Lrig1CreER^{T2}:R26RConfetti:HPV8-E6tg compared to Lrig1CreER^{T2}:R26RConfetti:WT (Figure 4D). RNA sequencing of flow-sorted populations showed that a relatively small number of DEGs (533) differentiated Lrig1$^+$ confetti$^+$ from Lrig1CreER^{T2}:R26RConfetti:HPV8-E6tg and Lrig1CreER^{T2}:R26RConfetti:WT mice (Figure 4E and Supplemental Figure 3A; Supplemental Tables 2 and 3), but more than twice as much (212) as in the reciprocal comparison between HPV8-CERtg and WT mice (Figure 2A); suggesting that the other early region genes may mitigate against the effect of E6. Consistent with the expansion and migration of Lrig1$^+$ JZSC into the overlying epidermis, GSEA identified STAT3, EMT (Figure 4F) and stem cell proliferation, but not differentiation or MYC (Supplemental Figure 3B) gene signatures in the comparison of the Lrig1$^+$ confetti$^+$ populations. A larger number of DEGs (6087) distinguished the Lrig1$^-$ confetti$^+$ populations,

wherein GSEA similarly identified STAT3, EMT but not differentiation (Figure 4G), as well as stem cell and migration (Supplemental Figure 3C) gene signatures in the HPV-E6tg population. Surprisingly, GSEA of HPV8-E6tg Lrig1^{+} confetti^{+} vs Lrig1^{-} confetti^{+} identified negative enrichment for STAT3, but no difference in EMT gene signatures, suggesting that STAT3 transcriptional node activation was still evident within the Lrig1 progeny (Figure 4H). Consistent with STAT3 activation in the Lrig1^{+} JZSC and their progeny in HPV8-E6tg, there was a large overlap in DEGs when these populations are compared to WT (Supplemental Figure 3D). Comparison of HPV8-E6tg Lrig1^{+} confetti^{+} and Lrig1^{-} confetti^{+} demonstrated similar expression levels of STAT3-regulated genes compared to their WT counterparts (Figure 4I). Consistent with retained KSCs within the HPV8-E6tg Lrig1^{+} JZSC progeny, we determined no difference in CFE between HPV8-E6tg Lrig1^{+} confetti^{+} and Lrig1^{-} confetti^{+} keratinocytes (Figure 4J). Hence, HPV8-E6 induced selective proliferation of Lrig1^{+} JZSC that led to expansion of KSCs into the overlying infundibulum and epidermis.

E6 bound P300 activates the STAT3 regulatory node

To determine how the HPV8 E6 protein might activate the STAT3 regulatory node, we used the previously reported stably transduced human keratinocytes, HaCaT (Figure 5) and PM1 (Supplemental Figure 4)(50, 51). Consistent with our findings in the HPV8-CERtg and HPV8-E6tg mouse keratinocytes, but in contrast to vector control and E7, the E6-transduced HaCaT cells demonstrated higher levels of pSTAT3 Y705 when looking at nuclear protein fractions (Figure 5A). Likewise, E6-transduced HaCaT cells, but not E7-transduced HaCaT cells, exhibited increased expression of STAT3 downstream target genes; including *ΔNp63* (Figure 5B and Supplemental Figure 4A). When cultured keratinocytes were subjected to higher calcium concentrations to simulate epidermal differentiation, E6-transduced cells maintained ΔNp63 expression and exhibited delayed expression of the differentiation marker involucrin, compared to vector control and E7-transduced cells (Figure 5C). There was no difference in proliferation (Figures 5D and Supplemental Figure 4B), however, HPV8 E6-transduced keratinocytes demonstrated 1.5-

fold greater CFE when compared to vector control and E7 (Figure 5E and Supplemental Figure 4C). Consistent with the egress of HPV8 Lrig1^{+} JZSCs, E6-transduced human keratinocytes migrated significantly faster when compared to vector only and E7-transduced cells (Figure 5F and Supplemental Figure 4D). Therefore, E6-transduced human keratinocytes demonstrated activation of the STAT3 regulatory node, which regulates the expression of *ΔNp63*, increasing KSC and migratory potential.

Across several HPV genotypes E6 binding partners have been identified using immunoprecipitation and mass spectroscopy, of which HPV8 E6 bound 7 proteins: EP300 (P300), CREB binding protein, SMAD3, LRP1, LRRC15, MAML1 and NOTCH1 (52). String™ analysis identified two related histone acetyltransferase proteins that regulate transcription via chromatin remodeling and also acetylate STAT3, thereby enhancing its transcriptional activity: P300 (Combined Score:0.986) and CREB binding protein (Combined Score:0.967)(53–60) (Figure 5G and Supplemental Figure 4). HPV8 E6 has a relatively unique 132-136 amino acid sequence that directly facilitates binding to the ubiquitously expressed related paralog transcriptional co-activators P300 and CREB binding protein (61). A single amino acid substitution, HPV8 E6 K136N, could block P300 binding and in transgenic mice expressing this mutant E6 prevent papilloma formation after UVB exposure (62). Here we show that HPV8 E6 K136N mutation did not induce STAT3 Y705 phosphorylation (Supplemental Figure 4E) nor increase ΔNp63 expression (Supplemental Figure 4F). Furthermore, mice expressing HPV8 E6 K136N demonstrated normal levels of Tyr705 STAT3 phosphorylation compared to native HPV8 E6 (Supplemental Figure 4G). P300 was ubiquitously expressed in HPV8 mouse keratinocytes (Figure 5H) and transduced human keratinocytes (Figure 5I and Supplemental Figure 4H). Knockdown of P300 expression by siRNA, decreased STAT3 Y705 phosphorylation and ΔNp63 expression (Figure 5J, Supplemental Figure 4K). Likewise, knockdown of STAT3 also led to a reduction in ΔNp63 expression (Figure 5K, Supplemental Figure 4L). Total STAT3 immunoprecipitation of nuclear extracts showed a greater amount of acetylated STAT3 in

E6 compared to vector control (Figure 5L). Consistent with these findings, STAT3 chromatin immunoprecipitation confirmed enriched binding of endogenous STAT3 to the putative STAT3-responsive element within the 5'-flanking region ΔNp63 promoter in E6-transduced cells relative to vector control cells (Figure 5M). Hence, HPV8 E6 binding to P300 is necessary for activation of the STAT3 regulatory node.

YAP contributes to STAT3 regulated *ΔNp63* expression.

KSCs demonstrate nuclear YAP translocation, as diminished Hippo signaling leads to unphosphorylated YAP translocating into the nucleus where it can interact with STAT3 to participate in transcription (63). To determine if nuclear YAP was essential for HPV8 E6-induced Lrig1$^+$ JZSC proliferation, we first determined that nuclear YAP was increased in nuclear protein extracts from Lrig1$^+$ flow sorted HPV8-E6tg vs WT mouse skin and E6-transduced HaCaT cell line by Western blot (Figure 6A and B, respectively). YAP siRNA knockdown in E6-transduced HaCaT cells, but not vector control cells, led to a reduction in Tyr705 STAT3 phosphorylation (Figure 6C and Supplemental Figure 5, respectively). As nuclear translocation of YAP has previously been reported when cells are cultured sparsely, we similarly observed nuclear YAP within sparsely cultured E6-transduced HaCaT cells, relative to vector control, wherein it co-localized with Tyr705 STAT3 phosphorylation and ΔNp63 expression (Figure 6D). Furthermore, immunoprecipitation of YAP nuclear protein extracts from E6-transduced HaCaT cells grown at ~50% confluence demonstrated higher levels of bound STAT3 and ΔNp63 compared to vector control, suggesting that YAP may be a co-transcription factor for both STAT3 and ΔNp63 (Figure 6E). Knockdown of YAP reduced HPV8 E6 induced cell proliferation (Figure 6F). Hence, HPV8-E6tg KSC proliferation was dependent upon YAP as an essential co-factor for STAT3 and ΔNp63 transcription.

HPV8 is associated with human actinic keratoses

HPV8 has been linked with keratoses and cSCC in patients with the primary immunodeficiency syndrome EV, wherein koilocytes are present, and in other forms of immunosuppression. Thus, we hypothesized that the presence of koilocytes in AK may indicate HPV8 reactivation within the general population, from immunosuppression associated with aging and/or sun exposure. Of 275 patients with pathologist-defined AK, we determined the presence of koilocytes in haematoxylin and eosin-stained tissue samples in 193 (70%) (Figure 7A). Using a representative subset of 77 cases (44 with koilocytes), we determined that the presence of koilocytes in AK was not associated with significant differences in age, sex (Fisher's exact test, NS), body location or histological classifications (Supplemental Table 4). To determine the presence of HPV8, we used a β-HPV L1 open reading frame PCR-reverse hybridisation assay (detects 25 β-HPV types), DNA analysis by nested PCR and tissue immunofluorescence for HPV8 E4 protein (Supplemental Figure 6A). The PCR-reverse hybridisation assay, which has been reported to be the most sensitive assay (64), identified 6 of 43 HPV8 positive samples with a high yield (>100 DNA copies per cell) and 37 of 43 HPV8 positive samples with low yield (no HPV47 was detected). The presence of koilocytes within AK was 100% sensitive for HPV8 with a 98% positive predictive value. In the remaining koilocyte AK case, HPV38 was detected, whereas in the absence of koilocytes in AK no β-HPV types were detected (Figure 7A). Thus, AK koilocytes predicted the detection of HPV8. Consistent with HPV8 E7-mediated ubiquitination and proteasomal degradation (Supplemental Figure 6B), AK samples with koilocytes had lower levels of Rb1 protein (Figure 7B), even though p16 expression showed no difference (Supplemental Figure 6C). We observed a much greater frequency of nuclear pSTAT3 Y705 labeling within the epidermis of koilocyte containing AK than without, 23.10±3.38% vs 7.68±2.92%, respectively (Figure 7C). In normal skin, p63 antibody labeling identified basal cells, but in AK, suprabasal p63 labeling was observed in the HF infundibulum and adjoining epidermis (Figure 7D). The frequency of p63 labeling was

marginally greater among AK with koilocytes (Figure 7D). Although the detection of HPV8 DNA does not necessarily infer viral reactivation, the presence of koilocytes in AK associated with reduction in Rb1 is highly suggestive.

Human epidermal keratinocytes are protected from UV-induced DNA damage by melanosomes transferred from adjacent melanocytes, which forms a “melanin” cap over the nucleus. We therefore hypothesized that the constant proliferation and translocation of JZSCs into the adjoining epidermis may lessen melanosome protection. Compared to normal skin, melanin staining was absent in all AK, irrespective of the presence of koilocytes (Figure 7E). Thus, since the absence of melanosomes is common, next we studied the DNA damage response to DNA double-strand breaks, which involves phosphorylation of the histone variant H2AX at serine 139 in the flanking regions of chromatin and can be labeled with specific antibodies that form visible foci in mammalian cells (65). The percentage of nuclei with phosphorylated H2AX labeling was much greater in AK with koilocytes than without, 92.43$\pm$3.97% vs 53.86$\pm$8.40%, respectively (Supplemental Figure 6D). UV frequently mutates p53 in human AK, as expected there was no difference in the frequency of nuclear p53 in AK, with (41.10$\pm$6.36%) and without (36.46$\pm$5.34%) koilocytes in the epidermis (Figure 7F); similarly, there was no difference in p21 labeling (Supplemental Figure 6E). Hence based on the HPV8-CERtg mouse model, in human AK with koilocytes, HPV8 may also activate pSTAT3 to drive p63 expression leading to HF junctional zone expansion and displacement without melanin protection into the overlying UV-exposed epidermis (Supplemental Figure 6F).

Discussion

The mammalian skin contains several adult tissue stem cell populations, wherein the Lrig1$^+$ JZSC represents a transcriptionally distinct population (45, 66). Although Lrig1 expression itself has been used to identify a number of adult stem cell populations in different tissues (46, 67–71). Lrig1 is a negative regulator of epidermal growth factor receptor (EGFR) signaling and therefore promotes stem cell quiescence by binding to EGFR, causing its ubiquitination and proteasomal degradation (72, 73). Furthermore, EGFR signaling activates the c-Myc transcriptional node resulting in Lrig1 expression, such that Lrig1 expression represents an autoregulatory negative feedback loop (46, 72, 74). Loss of Lrig1 expression in the skin leads to autonomous JZSC proliferation with increased cell numbers in the overlying HF infundibulum and perifollicular epidermis (46, 75). During homeostasis, as shown in our Lrig1CreER^{T2}:R26RConfetti model, the Lrig1$^+$ JZSC population contributes to the maintenance of cell numbers in the sebaceous gland and infundibulum (68, 76, 77). In keeping with this, it has also been proposed that Lrig1 JZSC transformation is the basis for sebaceous carcinoma (78). Thus, during homeostasis, the Lrig1$^+$ JZSCs represents a tightly regulated distinct functional HF population.

Here we have shown that HPV8 early region genes, which are shared by other HPV across the genera, specifically circumvent the Lrig1$^+$ JZSC c-Myc regulatory node to induce proliferation and KSC expansion into the interfollicular epidermis. The c-Myc transcriptional node clearly distinguishes the Lrig1$^+$ JZSCs from the CD34$^+$ HF bulge KSC population, even in the context of HPV8 early region gene expression. Herein we describe an alternative pathway for Lrig1+ JZSC proliferation governed by the STAT3 regulatory node signaling through downstream target genes, which include *c-Myc* and *ΔNp63*. This pathway, which is only activated in the Lrig1 JZSC population, is driven by HPV8 E6 protein interaction with P300, which activates STAT3. Importantly, we show that STAT3 activation

causes the proliferation and expansion of KSCs through increased symmetric cell division, allowing KSCs to be displaced from their niche into the interfollicular epidermis. Moreover, it appears that Lrig1 is an important, but pleotropic factor that inhibits STAT3 and multiple other growth factor receptors from signaling; including c-Met (79), RET (80), neurotrophic receptor tyrosine kinase 2 (TrkB, NRTK2)(81), TNFα (82), and androgen receptors (83). Corneal wounding, in the absence of Lrig1, led to STAT3 activation and premature corneal opacification (84). Whether STAT3 regulatory node activation in the Lrig1 JZSC population is responsible for the transient transfer of KSCs into the interfollicular epidermis after injury, since epidermal loss of STAT3 is associated with delayed wound healing, remains to be determined (85–87). In the context of HPV, this mechanism may allow the virus to reside in a protected JZSC population and upon reactivation still release virons via the overlying interfollicular epidermis.

STAT3 activation, which is associated with cytokine signaling in immune cells, has been observed in several malignancies, both within cancer cells, but also, within the tumor microenvironment immune cells (88). Numerous oncogenic signaling pathways converge to give rise to constitutive STAT3 activation, although less frequent STAT3 oncogenic mutations occur in myeloproliferative and skin malignancies (89). Inhibitors of the IL-6/JAK/STAT3 pathway are already in clinical use, and novel STAT3 selective inhibitors are currently in development. Constitutive activation of STATs, in particular STAT3, is found in carcinoma from the head and neck (90), lung (91), breast (92), ovary (93), and prostate (94). Within the context of cSCC, STAT3 deficiency is sufficient to block tumor formation in the two-step chemical skin cancer mouse model, wherein tumors develop from within the HF bulge KSC population (95). Although not described in the context of the Lrig1 JZSC population, constitutive expression of activated STAT3 in the skin leads to keratinocyte proliferation and expansion, similar to what we have observed in the

Lrig1CreER^{T2}:R26RConfetti:HPV8-CERtg but not in the Krt15CrePGR:R26RConfetti:HPV8-CERtg mice, with increased susceptibility for UV-induced transformation (96). Consistent with the importance of STAT3 signaling in HPV8, HPV8-CER:STAT3$^{+/-}$tg mice did not demonstrate Lrig1^{+} JZSC expansion nor tumorigenesis.

HPV8 E6 exhibits intrinsic oncogenic activity (43), but unlike αHPV it does not bind and inactivate p53 by rapid proteasome-mediated degradation; although it may prevent its stabilisation (97, 98). Multiple studies have demonstrated the ability of HPV8 to bind p300 (52, 61, 62, 99, 100). The ability of HPV8 E6 to transform keratinocytes has been studied for other binding partners impacting tumor suppressor and oncogenic pathways: Notch (101–103), TGFβ (104), Hippo (105), EGFR (106) and Wnt (107). In addition to the ability of HPV8 E6 bound p300 to activate the STAT3 pathway, as described herein, the association has been shown to attenuate activation of two essential DNA repair kinases ATM and ATR (108). We and others have shown HPV8-associated impaired DNA repair, which would facilitate the acquisition of transforming mutations (40, 109, 110).

HPV8 reactivation associated JZSC proliferation and expansion mirrors the pathological findings in human AK (38). While the presence of koilocytes in AK has been reported, their presence has previously been attributed to UV-induced transformation. Here we show that the presence of koilocytes in AK is indicative of HPV8, with loss of Rb1 and increased STAT3 phosphorylation. Although HPV8 E7 demonstrated lower binding of Rb1 and does not directly cause degradation, we have previously shown reduced Rb1 levels in human keratinocytes expressing E7 and all the complete early region genes (111–113). The archetypal AK pathology findings include a dilated HF infundibulum with overlying orthokeratosis and an accumulation of atypical keratinocytes within the perifollicular epidermis (114). As would be expected from viral reactivation, AK are frequently observed

with a dense inflammatory cell infiltrate. While in our mouse models constitutive expression of the HPV8 early region genes results in JZSC proliferation and expansion into the overlying interfollicular epidermis, the ensuing immune response is able to restore equilibrium in native infection. Thus, explaining the increased risk of AK in immune-suppressed individuals and similarly why in otherwise healthy individuals, 87% of AK spontaneously resolve within four-years (115). Herein we hypothesize that JZSC proliferation and expansion into the overlying interfollicular epidermis occurs in the absence of melanin protection, such that these keratinocytes easily accrue UV-induced mutations; thus, providing a basis for the “hit and run” mechanism. Consistent with this we observed p21 and p53 clones throughout the AK epidermis, and H2AX phosphorylation. In conclusion, our findings in the context of HPV8 reactivation redefine human AK as a HF disorder of KSCs and provides a mechanistic explanation for the ‘hit and run’ hypothesis for HPV8 induced cSCC.

Methods

Further information can be found in Supplemental Methods

Sex as a biological variable

For both human and animal models in this study, male and female samples were used, and similar findings were reported for both sexes.

Experimental Models

Mice

B6.129P2-*Gt(ROSA)26Sor*$^{tm1(CAG-Brainbow2.1)Cle}$/J ,(44, 116) *Lrig1*$^{tm1.1(cre/ERT2)Rjc}$/J,(117) B6;SJL-Tg(Krt1-15-cre/PGR*)22Cot/J(118) were purchased from the Jackson Laboratory. Lrig1-EGFP-ires-CreER^{T2} mice were a kind gift from Kim Jensen (University of Copenhagen, Denmark)(46). Krt14-HPV8-CER,(39) Krt14-HPV8-E2,(42) Krt14-HPV8-E6,(43) and Krt14-HPV8-E7(41) mice were used in this study. B6.129P2-*Gt(ROSA)26Sor*$^{tm1(CAG-Brainbow2.1)Cle}$/J, *Lrig1*$^{tm1.1(cre/ERT2)Rjc}$/J, B6;SJL-Tg(Krt1-15-cre/PGR*)22Cot/J and Lrig1-EGFP-ires-CreER^{T2} mice were backcrossed with FVBN mice for six generations to yield a pure FVBN background and finally interbred with Krt14-HPV8-CER and Krt14-HPV8-E6 mice. Stat3$^{WT/LoxP}$/FVBN and Stat3$^{WT/WT}$/FVBN mice were crossed with Krt14-HPV8-CER mice to generate Stat3$^{WT/LoxP}$/Krt14-HPV8/FVBN and Stat3$^{WT/WT}$/Krt14-HPV8/FVBN mice.

Tamoxifen and RU486 injection

Cre activation in Lrig1CreER^{T2} mice was induced by injecting 4-week-old mice intraperitoneally with 80 mg/kg/day of tamoxifen in corn oil for four consecutive days. Cre activation in Krt15CrePGR mice was induced by injecting 4-week-old mice intraperitoneally

with 80 mg/kg/day of RU486 in corn oil for four consecutive days. Mice were harvested 30 days post induction.

Cell lines

Three established cell lines; HaCaT, PM1 and J2-3T3 were used in this research. Details on cell culture conditions used can be found in the Supplemental Methods.

Methods Details

Generation of transduced HaCaT and PM1 cell lines

The Moloney murine leukemia retrovirus vector pLXSN (vector control) was used to generate recombinant retroviruses containing HPV8 genes coding for HPV8 E6 and E7. Briefly, retroviral transduction of HaCaT and PM1 cell lines were performed by seeding cells into 6cm dishes, allowed to adhere overnight, before adding a mixture of retroviral supernatants with an equal volume of DMEM in the presence of 5 μg/mL of hexadimethrine bromide (polybrene). Spin infection was made by centrifugation for 1 hour at 300xg. Cells were washed with PBS and cultured for two days before being selected for using G418 at a concentration of 500 μg/mL.

Tissue dissociation and culture

Mouse dorsal back skin was dissociated into single cells as described previously (38).

Murine primary colony forming assay culture

Mouse dorsal back skin was dissociated into single cells as described above. Lrig1 expressing mouse keratinocytes were isolated through flow sorting and 2,500 cells were seeded on an irradiated J2-3T3 feeder layer per well in a 6-well plate and cultured in

Rheinwald and Green media for 15 days, with media changed every 3 days. The colonies were stained with crystal violet, scanned with a GelCount machine (Oxford Optronix, Abingdon, UK) and quantified using ImageJ software (NIH, Bethesda, MD).

Short interfering RNA knockdown experiments

siRNA transfections were performed 24 hours after seeding keratinocytes with siRNA (ON-Targetplus SMARTpool, Dharmacon), Lipofectamine 3000 transfection reagent (ThermoFisher Scientific) and Opti-MEM (ThermoFisher Scientific). siRNA concentrations were optimized individually. Cell lines were transfected with siRNA targeting STAT3 (20ηM), P300 (30ηM), YAP (20ηM).

Calcium shift experiment on established cell lines

Keratinocytes were de-differentiated by culturing cells for 48 hours in Epilife media (containing no calcium chloride; MEPICF500). Keratinocytes were induced to differentiate by adding Epilife media (containing 60μm calcium final concentration) and left for the number of days stated in the figure to assess differentiation levels.

Whole mount skin preparation and fluorescence imaging

Tail skin was cut into 0.5cm^2 pieces and placed overnight at 4°C in Dispase (2.5U/mL). Epidermis was gently removed from the underlying dermis using forceps and fixed in 10% neutral buffered formalin for 90 minutes at room temperature. Tissue was washed in PBS and stored in PBS+0.2% sodium azide at 4°C ready for immunofluorescence labelling. Immunofluorescence on tail skin was performed as described previously (38). Antibodies used can be found in Supplemental Table 5.

626 **Immunofluorescence staining and microscopy of OCT sections**

627 Immunofluorescence was performed on either frozen OCT embedded or paraffin embedded
628 sections as previously described (38). Further experimental details and antibodies used can
629 be found in the Supplemental Methods and Supplemental Table 5, respectively.
630

631 **Immunohistochemistry staining**

632 Rehydration of sections and antigen retrieval was performed as described in the
633 immunofluorescence staining above. Further experimental details and antibodies used can
634 be found in the Supplemental Methods and Supplemental Table 5, respectively.
635

636 **Starry-Warthin stain**

637 All reaction solutions were reduced from pH 4 to pH 3.2 before conducting the staining as
638 per manufacturer's instructions (Abcam, UK).

639

640 **Fluorescence-activated cell sorting (FACS) or analysis**

641 Samples were analyzed and flow sorted using BD LSR Fortessa and BD FACSAria Fusion
642 (BD Biosciences), respectively. Mouse telogen dorsal back skin was dissociated and
643 washed with FACS buffer (0.05% sodium azide and 0.5% BSA in PBS) before primary
644 antibody staining for 30 minutes on ice. Primary antibodies used in this study: Lrig1 488
645 (R&D systems, FAB3688G), Lrig1 647 (VWR, 10330-520), CD34 PE (BD, 551387).
646 Unbound antibodies were removed by washing with FACS buffer twice by centrifugation. All
647 centrifugations were performed at 250×g for 5 minutes at 4°C. Details on the gating
648 strategy can be found in the Supplemental Methods

649

Western immunoblotting

Whole protein lysate was extracted using Lysing Matrix D tubes (MP Biomedicals) by homogenization for tissue or agitation with a pipette for cell pellets in RIPA buffer (ThermoFisher Scientific) supplemented with 1x protease/phosphatase inhibitor cocktail (Cell Signalling). Nuclear protein lysate was extracted using NE-PER™ Nuclear and Cytoplasmic Extraction reagents (ThermoFisher Scientific). Details on how Western blotting was performed and the antibodies used can be found in the Supplemental Methods and Supplemental Table 5, respectively.

Co-Immunoprecipitation

Nuclear protein lysates were prepared from HaCaT cells at a confluency of 50-60%. Co-IP experiments were performed using the Pierce™ Co-Immunoprecipitation kit (ThermoFisher Scientific). Further details on how Co-Immunoprecipitation was performed can be found in the Supplemental Methods.

Chromatin Immunoprecipitation (ChIP)-qPCR

ChIP-qPCR experiment was performed using the High-Sensitivity ChIP kit (Abcam) as per manufacturers guidelines. Further details on how ChIP-qPCR was performed can be found in the Supplemental Methods.

Colony forming ability (established cell lines)

HaCaT/PM1-PLXSN, -E6 and -E7 cells were seeded at a low density of 500 cells/well in a 6-well plate and left for 7 days in growth media to allow colonies to form. Colonies were quantified by removing the media, washing with PBS and staining with crystal violet solution

for 15 minutes on a rocker at room temperature, before washing off solution by gently running the plates under tap water. Plates were scanned and enumerated using a GelCount plate reader (Oxford Optronix).

RNA extraction and cDNA synthesis

Depending on cell numbers, RNA was isolated using the Qiagen RNeasy Plus Mini or Micro Kits (Qiagen, UK) per manufacturer's instructions. The quality of the extracted RNA was assessed using the Agilent RNA 6000 Nano kit. Agilent Nano chips where run on the Agilent 2100 Bioanalyzer according to manufacturer's guidelines. cDNA synthesis was performed using the Quantitect Reverse Transcription Kit (Qiagen, UK) in 0.2 mL PCR tubes as per manufacturer's instructions.

Quantitative real-time PCR (qPCR)

For qPCR gene expression studies, reactions were performed using TaqMan gene expression probes. Pre-designed TaqMan primer/probes were obtained from Applied Biosystems (see Supplemental Table 5). Reactions were run using the TaqMan Universal Master Mix II (Applied Biosystems) according to the manufacturer's guidelines. Housekeeping genes (GAPDH and β-actin) were used as reference genes. All reactions were run in three technical triplicates, and all experiments were performed at least three times independently. All reactions were run on the QuantStudio 7 Flex Real-Time PCR system (Applied Biosystems) supplemented with the QuantStudio software. Gene expression analysis of qPCR data was analyzed using the ΔΔCt method to calculate fold change ($2^{\wedge -\Delta\Delta Ct}$) relative to control.

DNA extraction, precipitation and β-HPV genotyping PCR

DNA was extracted from 25mg of FFPE sections using the QIAamp DNA Mini Kit (Qiagen, UK). For human samples with a DNA concentration <10 ηg/μL, DNA precipitation was performed to gain a higher concentration and purity. To perform genotyping, the PM-PCR Reverse Hybridisation Assay method was performed using RHA kit Stain (β) HPV kit (Labo Bio-Medical Products BV). Details can be found in the Supplemental Methods.

Nested PCR for HPV8 E6

The molecular detection of HPV8 in the skin tissue samples was performed using nested-PCR amplification. DNA was extracted from 44 FFPE samples exhibiting koilocytes and 33 FFPE samples with no koilocytes. Two sets of primers were designed, outer and nested. Both outer and nested sets were flanking an area in E7-E1 region of HPV8. Details on primer sequences and PCR reaction specifications can be found in the Supplemental Methods.

RNA sequencing of mouse dorsal back skin samples

RNA for RNA-seq was extracted and RNA quality was assessed as mentioned previously. Upper hair follicle (Lrig1) and bulge (CD34) stem cells were isolated by flow sorting from telogen dorsal back skin in 7-week-old Krt14-HPV8-CER and WT mice. Twelve samples (3x Lrig1+ WT, 3x Cd34+ WT, 3x Lrig1+ Krt14-HPV8-CER, 3x Cd34+ Krt14-HPV8-CER) were sequenced (GSE248056) by Wales Gene Park (WGP). Confetti-positive cells with and without Lrig1 cell surface expression were flow sorted from Lrig1CreER^{T2}:R26RConfetti:HPV8-E6tg and Lrig1CreER^{T2}:R26RConfetti:WT mice. Twelve samples (3x HPV8-E6tg Lrig1^{-}Confetti^{+}, 3x HPV8-E6tg Lrig1^{+}Confetti^{+}, 3x WT Lrig1^{-}Confetti^{+}, 3x WT Lrig1^{+}Confetti^{+}) were sequenced (GSE248056). Total RNA was extracted using an RNeasy Micro Kit (Qiagen). RNA was then frozen at -80°C and shipped to

Novogene (Cambridge, UK) on dry-ice for library preparation and sequencing. Further details on bioinformatic analyses can be found in the Supplemental Methods.

QUANTIFICATION AND STATISTICAL ANALYSIS

Statistics and reproducibility

Statistical analyses were performed in GraphPad Prism v9. Data are presented as mean ± SEM. Two-tailed Student's t-test was used to measure significance between two groups, while one-way ANOVA was used when comparing multiple groups. Specifically, statistical tests applied for each figure can be found in Supplemental Information. p-values <0.05 are considered significant. Symbols for significance: ns, non-significant, *, <0.05; **, <0.01; ***, <0.001; ****, <0.0001. For each experiment, n represents the number of experimental replicates. For animal experiments, age- and sex-matched mice were randomly assigned to groups, and at least three biological replicates were used for each experiment.

Identification of koilocyte-like keratinocytes

Human FFPE AK tissues (n=77) were serially sectioned with the first section stained with H&E and imaged. Each image was then carefully assessed for the presence of koilocytes in the epidermis. A sample was determined to be positive if multiple koilocytes were observed within 100 μm of epidermis as single entities or clusters.

Quantifying positively stained tissue sections

To determine positive cell expression, images were analysed using Qupath software (119). For pp53, p63, pSTAT3, p21, Rb1, p16 and pH2AX, the number of cells were determined using the automated cell detection tool; nuclei with either a haematoxylin or DAB optical

density over the defined intensity threshold were counted and those with a DAB value over the pre-determined positive threshold value defined as positive cells.

Study Approval

Animals. All mouse experiments carried out in this study were performed in accordance with a UK Home Office Licence (project license 30/3382).

Patient samples. Human tissue samples were obtained after informed written consent from patients following NHS Research and Development and Regional Ethics Committee approval (19/NS/0012). Pathologist diagnosed actinic keratosis samples together with anonymised clinical reports were collected. 275 patient samples were analyzed for the presence of koilocytes by histology, with a prospective cohort of the first 77 samples further studied in more detail for the presence of HPV8 via genotyping.

Data and code availability

RNA sequencing data have been deposited at GEO and are publicly available from the date of publication. Accession number is GSE248056. This paper does not report original code. Data are available in the “Supporting data values” XLS file. The lead contact can provide any additional information required to reanalyze the data within this paper.

Author contributions

GKP, BA, and MG conceived and supervised this study. GKP, HJM, CO, and BYS designed the experiments. HJM and CO performed *in vitro* and protein experiments. HJM, CO, and BYS performed *in vivo* experiments. AG, HJM, and CO performed bioinformatic analyses on RNA-seq datasets. HJM, CO, AG, ALP, LA, and AL performed work on human AK samples; LM and CB performed *in vivo* experiments and mouse tissue processing. MDA, MH, BA, and MG contributed new reagents and expertise throughout the project; GKP and RG conducted the human study; HJM, CO, BYS analyzed the data; GKP, HJM and CO wrote the manuscript. All authors edited the manuscript. The order of co–first authorship was determined by effort in data analysis and drafting the manuscript.

Acknowledgements

We would like to thank: 1) Leo Foundation (LF-OC-17-0070 and LF-OC-19-000083), 2) Marie Curie Horizon 2020 EU fellowship (799829; SKin SCiENCE) and 3) British Skin Foundation small grant for funding this work. We would like to thank the Wales Gene Park (Health and Care Research Wales) for their bioinformatic support. We would also like to thank Kim Jensen (Novo Nordisk Foundation Center for Stem Cell Medicine, Faculty of Health and Medical Sciences, University of Copenhagen, Copenhagen N DK-2200, Denmark) for providing the Lrig1-EGFP-ires-CreER^{T2} mouse model, and Sigrun Smola (Institute of Virology, Center of Human and Molecular Biology Building, Saarland University D-66421 Homburg Saar, Germany) for the transduced PM1 cell lines. We thank Dr Majid Rashid, a pathologist at the Royal Gwent Hospital, for his help with clinical samples.

References

1. Hannigan GD, et al. The human skin double-stranded DNA virome: Topographical and temporal diversity, genetic enrichment, and dynamic associations with the host microbiome. *mBio*. 2015;6(5).

2. Saheb Kashaf S, et al. Integrating cultivation and metagenomics for a multi-kingdom view of skin microbiome diversity and functions. *Nat Microbiol*. 2022;7(1).

3. Kumata R, et al. A tissue level atlas of the healthy human virome. *BMC Biol*. 2020;18(1).

4. Doorbar J. The papillomavirus life cycle. *Journal of Clinical Virology*. 2005;32(SUPPL.).

5. Potočnik M, et al. Beta-papillomaviruses in anogenital hairs plucked from healthy individuals. *J Med Virol*. 2006;78(12).

6. Schneider I, et al. Eyebrow hairs from actinic keratosis patients harbor the highest number of cutaneous human papillomaviruses. *BMC Infect Dis*. 2013;13(1).

7. Boxman ILA, et al. Detection of human papillomavirus DNA in plucked hairs from renal transplant recipients and healthy volunteers. *Journal of Investigative Dermatology*. 1997;108(5).

8. Kobayashi T, et al. Choreographing Immunity in the Skin Epithelial Barrier. *Immunity*. 2019;50(3).

9. Kobayashi T, et al. Homeostatic Control of Sebaceous Glands by Innate Lymphoid Cells Regulates Commensal Bacteria Equilibrium. *Cell*. 2019;176(5).

10. Adachi T, et al. Hair follicle-derived IL-7 and IL-15 mediate skin-resident memory T cell homeostasis and lymphoma. *Nat Med*. 2015;21(11).

11. Nagao K, et al. Brief report: Requirement of TACE/ADAM17 for hair follicle bulge niche establishment. *Stem Cells*. 2012;30(8).

12. Saeidian AH, et al. Whole transcriptome-based skin virome profiling in typical epidermodysplasia verruciformis reveals α-, β-, and γ-HPV infections. *JCI Insight*. 2023;8(5).

13. Lisco A, et al. Treatment of Relapsing HPV Diseases by Restored Function of Natural Killer Cells. *New England Journal of Medicine*. 2021;385(10).

14. Tirosh O, et al. Expanded skin virome in DOCK8-deficient patients. *Nat Med*. 2018;24(12).

15. Pastrana D V, et al. Metagenomic Discovery of 83 New Human Papillomavirus Types in Patients with Immunodeficiency. *mSphere*. 2018;3(6).

16. Patel AS, et al. Exposure profiles and human papillomavirus infection in skin cancer: An analysis of 25 genus β-types in a population-based study. *Journal of Investigative Dermatology*. 2008;128(12).

17. Bangash HK, Colegio OR. Management of non-melanoma skin cancer in immunocompromised solid organ transplant recipients. *Curr Treat Options Oncol*. 2012;13(3).

18. Neale RE, et al. Human papillomavirus load in eyebrow hair follicles and risk of cutaneous squamous cell carcinoma. *Cancer Epidemiology Biomarkers and Prevention*. 2013;22(4).

19. Feltkamp MCW, et al. Seroreactivity to epidermodysplasia verruciformis-related human papillomavirus types is associated with nonmelanoma skin cancer. *Cancer Res*. 2003;63(10).

20. Nindl I, Rösl F. Molecular concepts of virus infections causing skin cancer in organ transplant recipients. *American Journal of Transplantation*. 2008;8(11).

21. Antonsson A, et al. The Ubiquity and Impressive Genomic Diversity of Human Skin Papillomaviruses Suggest a Commensalic Nature of These Viruses. *J Virol*. 2000;74(24).

22. Proby CM, et al. A case-control study of betapapillomavirus infection and cutaneous squamous cell carcinoma in organ transplant recipients. *American Journal of Transplantation*. 2011;11(7).

847 23. Zheng ZM, Baker CC. Papillomavirus genome structure, expression, and post-transcriptional
848 regulation. *Frontiers in Bioscience*. 2006;11(SUPPL. 1).

849 24. De Villiers EM, et al. Classification of papillomaviruses. *Virology*. 2004;324(1).

850 25. Mistry N, et al. Cutaneous and mucosal human papillomaviruses differ in net surface charge,
851 potential impact on tropism. *Virol J*. 2008;5.

852 26. Doorbar J, et al. Human papillomavirus molecular biology and disease association. *Rev Med*
853 *Virol*. 2015;25(S1).

854 27. Arbyn M, et al. EUROGIN 2011 roadmap on prevention and treatment of HPV-related
855 disease. *Int J Cancer*. 2012;131(9).

856 28. McBride AA, Warburton A. The role of integration in oncogenic progression of HPV-
857 associated cancers. *PLoS Pathog*. 2017;13(4).

858 29. Chahoud J, et al. Association between β-genus human papillomavirus and cutaneous
859 squamous cell carcinoma in immunocompetent individuals-a meta-analysis. *JAMA Dermatol*.
860 2016;152(12).

861 30. Quint KD, et al. Human Beta-papillomavirus infection and keratinocyte carcinomas. *Journal*
862 *of Pathology*. 2015;235(2).

863 31. Borgogna C, et al. Improved detection reveals active β-papillomavirus infection in skin lesions
864 from kidney transplant recipients. *Modern Pathology*. 2014;27(8).

865 32. Borgogna C, et al. Characterization of beta papillomavirus E4 expression in tumours from
866 Epidermodysplasia Verruciformis patients and in experimental models. *Virology*. 2012;423(2).

867 33. Dell'Oste V, et al. High β-HPV DNA loads and strong seroreactivity are present in
868 epidermodysplasia verruciformis. *Journal of Investigative Dermatology*. 2009;129(4).

34. Dang C, et al. E6/E7 expression of human papillomavirus types in cutaneous squamous cell dysplasia and carcinoma in immunosuppressed organ transplant recipients. *British Journal of Dermatology*. 2006;155(1).

35. Neagu N, et al. The role of HPV in keratinocyte skin cancer development: A systematic review. *Journal of the European Academy of Dermatology and Venereology*. 2023;37(1).

36. Weissenborn SJ, et al. Human papillomavirus-DNA loads in actinic keratoses exceed those in non-melanoma skin cancers. *Journal of Investigative Dermatology*. 2005;125(1).

37. Ferreira DA, et al. A "hit-and-run" affair – A possible link for cancer progression in virally driven cancers. *Biochim Biophys Acta Rev Cancer*. 2021;1875(1).

38. Lanfredini S, et al. HPV8 Field Cancerization in a Transgenic Mouse Model Is due to Lrig1+ Keratinocyte Stem Cell Expansion. *Journal of Investigative Dermatology*. 2017;137(10).

39. Schaper ID, et al. Development of skin tumors in mice transgenic for early genes of human papillomavirus type 8. *Cancer Res*. 2005;65(4).

40. Borgogna C, et al. Enhanced Spontaneous Skin Tumorigenesis and Aberrant Inflammatory Response to UVB Exposure in Immunosuppressed Human Papillomavirus Type 8–Transgenic Mice. *Journal of Investigative Dermatology*. 2023;143(5).

41. Heuser S, et al. The fibronectin/α3β1 integrin axis serves as molecular basis for keratinocyte invasion induced by βhPV. *Oncogene*. 2016;35(34).

42. Pfefferle R, et al. The human papillomavirus type 8 E2 protein induces skin tumors in transgenic mice. *Journal of Investigative Dermatology*. 2008;128(9).

43. Marcuzzi GP, et al. Spontaneous tumour development in human papillomavirus type 8 E6 transgenic mice and rapid induction by UV-light exposure and wounding. *Journal of General Virology*. 2009;90(12).

892 44. Snippert HJ, et al. Intestinal crypt homeostasis results from neutral competition between
893 symmetrically dividing Lgr5 stem cells. *Cell*. 2010;143(1).

894 45. Joost S, et al. Single-Cell Transcriptomics Reveals that Differentiation and Spatial Signatures
895 Shape Epidermal and Hair Follicle Heterogeneity. *Cell Syst*. 2016;3(3).

896 46. Jensen KB, et al. Lrig1 Expression Defines a Distinct Multipotent Stem Cell Population in
897 Mammalian Epidermis. *Cell Stem Cell*. 2009;4(5).

898 47. Subramanian A, et al. Gene set enrichment analysis: A knowledge-based approach for
899 interpreting genome-wide expression profiles. *Proc Natl Acad Sci U S A*.
900 2005;102(43):15545-15550.

901 48. Mootha VK, et al. PGC-1α-responsive genes involved in oxidative phosphorylation are
902 coordinately downregulated in human diabetes. *Nat Genet*. 2003;34(3):267-273.

903 49. De Andrea M, et al. Keratinocyte-specific stat3 heterozygosity impairs development of skin
904 tumors in human papillomavirus 8 transgenic mice. *Cancer Res*. 2010;70(20).

905 50. Boukamp P, et al. Normal keratinization in a spontaneously immortalized aneuploid human
906 keratinocyte cell line. *Journal of Cell Biology*. 1988;106(3).

907 51. Proby CM, et al. Spontaneous keratinocyte cell lines representing early and advanced stages of
908 malignant transformation of the epidermis. *Exp Dermatol*. 2000;9(2).

909 52. White EA, et al. Comprehensive Analysis of Host Cellular Interactions with Human
910 Papillomavirus E6 Proteins Identifies New E6 Binding Partners and Reflects Viral Diversity. *J*
911 *Virol*. 2012;86(24).

912 53. Hou T, et al. The STAT3 NH2-terminal domain stabilizes enhanceosome assembly by
913 interacting with the p300 bromodomain. *Journal of Biological Chemistry*. 2008;283(45).

914 54. Nakashima K, et al. Synergistic signaling in fetal brain by STAT3-Smad1 complex bridged by
915 p300. *Science (1979)*. 1999;284(5413).

55. Ray S, et al. Angiotensinogen gene expression is dependent on signal transducer and activator of transcription 3-mediated p300/cAMP response element binding protein-binding protein coactivator recruitment and histone acetyltransferase activity. *Molecular Endocrinology*. 2002;16(4).

56. Yuan ZL, et al. Stat3 dimerization regulated by reversible acetylation of a single lysine residue. *Science (1979)*. 2005;307(5707).

57. Gray MJ, et al. HIF-1α, STAT3, CBP/p300 and Ref-1/APE are components of a transcriptional complex that regulates Src-dependent hypoxia-induced expression of VEGF in pancreatic and prostate carcinomas. *Oncogene*. 2005;24(19).

58. Wang R, et al. Activation of Stat3 sequence-specific DNA binding and transcription by p300/CREB-binding protein-mediated acetylation. *Journal of Biological Chemistry*. 2005;280(12).

59. Sun Y, et al. Neurogenin promotes neurogenesis and inhibits glial differentiation by independent mechanisms. *Cell*. 2001;104(3).

60. He J, et al. Yes-associated protein promotes angiogenesis via signal transducer and activator of transcription 3 in endothelial cells. *Circ Res*. 2018;122(4).

61. Müller-Schiffmann A, et al. The E6 Protein of the Cutaneous Human Papillomavirus Type 8 Can Stimulate the Viral Early and Late Promoters by Distinct Mechanisms. *J Virol*. 2006;80(17).

62. Hufbauer M, et al. Human papillomavirus mediated inhibition of DNA damage sensing and repair drives skin carcinogenesis. *Mol Cancer*. 2015;14(1).

63. De Rosa L, et al. Laminin 332-Dependent YAP Dysregulation Depletes Epidermal Stem Cells in Junctional Epidermolysis Bullosa. *Cell Rep*. 2019;27(7).

64. De Koning M, et al. Evaluation of a novel highly sensitive, broad-spectrum pcr-reverse hybridization assay for detection and identification of beta-papillomavirus DNA. *J Clin Microbiol*. 2006;44(5).

65. Jackson SP, Bartek J. The DNA-damage response in human biology and disease. *Nature*. 2009;461(7267).

66. Joost S, et al. The Molecular Anatomy of Mouse Skin during Hair Growth and Rest. *Cell Stem Cell*. 2020;26(3).

67. Tan DWM, et al. Single-cell gene expression profiling reveals functional heterogeneity of undifferentiated human epidermal cells. *Development (Cambridge)*. 2013;140(7).

68. Page ME, et al. The epidermis comprises autonomous compartments maintained by distinct stem cell populations. *Cell Stem Cell*. 2013;13(4).

69. Schweiger PJ, et al. Lrig1 marks a population of gastric epithelial cells capable of long-term tissue maintenance and growth in vitro. *Sci Rep*. 2018;8(1).

70. Wong VWY, et al. Lrig1 controls intestinal stem-cell homeostasis by negative regulation of ErbB signalling. *Nat Cell Biol*. 2012;14(4).

71. Jensen KB, Watt FM. Single-cell expression profiling of human epidermal stem and transit-amplifying cells: Lrig1 is a regular of stem cell quiescence. *Proc Natl Acad Sci U S A*. 2006;103(32).

72. Ghiglione C, et al. The transmembrane molecule kekkon 1 acts in a feedback loop to negatively regulate the activity of the Drosophila EGF receptor during oogenesis. *Cell*. 1999;96(6).

73. Laederich MB, et al. The leucine-rich repeat protein LRIG1 is a negative regulator of ErbB family receptor tyrosine kinases. *Journal of Biological Chemistry*. 2004;279(45).

74. Dahlhoff M, et al. Overexpression of Epigen during Embryonic Development Induces Reversible, Epidermal Growth Factor Receptor-Dependent Sebaceous Gland Hyperplasia. *Mol Cell Biol*. 2014;34(16).

75. Suzuki Y, et al. Targeted disruption of LIG-1 gene results in psoriasiform epidermal hyperplasia. *FEBS Lett*. 2002;521(1-3).

76. Frances D, Niemann C. Stem cell dynamics in sebaceous gland morphogenesis in mouse skin. *Dev Biol*. 2012;363(1).

77. Gandarillas A, Watt FM. c-Myc promotes differentiation of human epidermal stem cells. *Genes Dev*. 1997;11(21).

78. Frances D, et al. A role for Rac1 activity in malignant progression of sebaceous skin tumors. *Oncogene*. 2015;34(43).

79. Shattuck DL, et al. LRIG1 Is a Novel Negative Regulator of the Met Receptor and Opposes Met and Her2 Synergy. *Mol Cell Biol*. 2007;27(5).

80. Ledda F, et al. Lrig1 is an endogenous inhibitor of ret receptor tyrosine kinase activation, downstream signaling, and biological responses to GDNF. *Journal of Neuroscience*. 2008;28(1).

81. Alsina FC, et al. Lrig1 is a cell-intrinsic modulator of hippocampal dendrite complexity and BDNF signaling . *EMBO Rep*. 2016;17(4).

82. Bai L, et al. LRIG1 modulates cancer cell sensitivity to smac mimetics by regulating TNFα expression and receptor tyrosine kinase signaling. *Cancer Res*. 2012;72(5).

83. Li Q, et al. LRIG1 is a pleiotropic androgen receptor-regulated feedback tumor suppressor in prostate cancer. *Nat Commun*. 2019;10(1).

84. Nakamura T, et al. LRIG1 inhibits STAT3-dependent inflammation to maintain corneal homeostasis. *Journal of Clinical Investigation*. 2014;124(1).

85. Plikus M V, et al. Epithelial stem cells and implications for wound repair. *Semin Cell Dev Biol*. 2012;23(9).

86. Sano S, et al. Keratinocyte-specific ablation of Stat3 exhibits impaired skin remodeling, but does not affect skin morphogenesis. *EMBO Journal*. 1999;18(17).

87. Ito M, et al. Stem cells in the hair follicle bulge contribute to wound repair but not to homeostasis of the epidermis. *Nat Med*. 2005;11(12).

88. Li YJ, et al. STAT proteins in cancer: orchestration of metabolism. *Nat Rev Cancer*. 2023;23(3).

89. Johnson DE, et al. Targeting the IL-6/JAK/STAT3 signalling axis in cancer. *Nat Rev Clin Oncol*. 2018;15(4).

90. Geiger JL, et al. The STAT3 pathway as a therapeutic target in head and neck cancer: Barriers and innovations. *Oral Oncol*. 2016;56.

91. Njatcha C, et al. STAT3 cyclic decoy demonstrates robust antitumor effects in non–small cell lung cancer. *Mol Cancer Ther*. 2018;17(9).

92. Ma JH, et al. Role of STAT3 signaling pathway in breast cancer. *Cell Communication and Signaling*. 2020;18(1).

93. Liang R, et al. STAT3 signaling in ovarian cancer: A potential therapeutic target. *J Cancer*. 2020;11(4).

94. Ebersbach C, et al. Impact of stat proteins in tumor progress and therapy resistance in advanced and metastasized prostate cancer. *Cancers (Basel)*. 2021;13(19).

95. Kataoka K, et al. Stage-specific disruption of Stat3 demonstrates a direct requirement during both the initiation and promotion stages of mouse skin tumorigenesis. *Carcinogenesis*. 2008;29(6).

96. Sano S, et al. Stat3 links activated keratinocytes and immunocytes required for development of psoriasis in a novel transgenic mouse model. *Nat Med*. 2005;11(1).

97. White EA, et al. Genus Beta Human Papillomavirus E6 Proteins Vary in Their Effects on the Transactivation of p53 Target Genes. *J Virol*. 2014;88(15).

98. Wallace NA, et al. Beta Human Papillomavirus E6 Expression Inhibits Stabilization of p53 and Increases Tolerance of Genomic Instability. *J Virol*. 2014;88(11).

99. Rozenblatt-Rosen O, et al. Interpreting cancer genomes using systematic host network perturbations by tumour virus proteins. *Nature*. 2012;487(7408).

100. Dacus D, Wallace NA. Beta-genus human papillomavirus 8 e6 destabilizes the host genome by promoting p300 degradation. *Viruses*. 2021;13(8).

101. Tan MJA, et al. Cutaneous β-human papillomavirus E6 proteins bind Mastermind-like coactivators and repress Notch signaling. *Proc Natl Acad Sci U S A*. 2012;109(23).

102. Meyers JM, et al. The Human Papillomavirus Type 8 E6 Protein Interferes with NOTCH Activation during Keratinocyte Differentiation. *J Virol*. 2013;87(8).

103. Brimer N, et al. Cutaneous papillomavirus E6 oncoproteins associate with MAML1 to repress transactivation and NOTCH signaling. *Oncogene*. 2012;31(43).

104. Meyers JM, et al. Inhibition of TGF-β and NOTCH signaling by cutaneous papillomaviruses. *Front Microbiol*. 2018;9(MAR).

105. Dacus D, et al. Beta Human Papillomavirus 8E6 Attenuates LATS Phosphorylation after Failed Cytokinesis. *J Virol*. 2020;94(12).

106. Taute S, et al. Induction of tyrosine phosphorylation of UV-activated EGFR by the beta-human papillomavirus type 8 E6 leads to papillomatosis. *Front Microbiol*. 2017;8(NOV).

1031 107. Wu SC, et al. The HPV8 E6 protein targets the Hippo and Wnt signaling pathways as part of
1032 its arsenal to restrain keratinocyte differentiation. *mBio*. 2023;14(5).

1033 108. Snow JA, et al. β-HPV 8E6 Attenuates ATM and ATR Signaling in Response to UV Damage.
1034 *Pathogens*. 2019;8(4).

1035 109. Dacus D, et al. β-HPV 8E6 combined with TERT expression promotes long-term proliferation
1036 and genome instability after cytokinesis failure. *Virology*. 2020;549.

1037 110. Dacus D, et al. Beta Human Papillomavirus 8 E6 Induces Micronucleus Formation and
1038 Promotes Chromothripsis. *J Virol*. 2022;96(19).

1039 111. Schmitt A, et al. Comparison of the properties of the E6 and E7 genes of low- and high-risk
1040 cutaneous papillomaviruses reveals strongly transforming and high Rb-binding activity for the
1041 E7 protein of the low-risk human papillomavirus type 1. *J Virol*. 1994;68(11).

1042 112. Yamashita T, et al. Biological and biochemical activity of E7 genes of the cutaneous human
1043 papillomavirus type 5 and 8. *Oncogene*. 1993;8(9).

1044 113. Akgül B, et al. HPV8 early genes modulate differentiation and cell cycle of primary human
1045 adult keratinocytes. *Exp Dermatol*. 2007;16(7).

1046 114. Elder DE, et al. WHO Classification of Skin Tumours, Volume 11. In: *Skin Tumours.*
1047 *Pathology and Genetics. Lyon (France): IARCPress.* ; 2018.

1048 115. Criscione VD, et al. Actinic keratoses: Natural history and risk of malignant transformation in
1049 the veterans affairs topical tretinoin chemoprevention trial. *Cancer*. 2009;115(11).

1050 116. Livet J, et al. Transgenic strategies for combinatorial expression of fluorescent proteins in the
1051 nervous system. *Nature*. 2007;450(7166).

1052 117. Powell AE, et al. The pan-ErbB negative regulator lrig1 is an intestinal stem cell marker that
1053 functions as a tumor suppressor. *Cell*. 2012;149(1).

118. Morris RJ, et al. Capturing and profiling adult hair follicle stem cells. *Nat Biotechnol*. 2004;22(4).

119. Bankhead P, et al. QuPath: Open source software for digital pathology image analysis. *Sci Rep*. 2017;7(1):1-7.

Figures

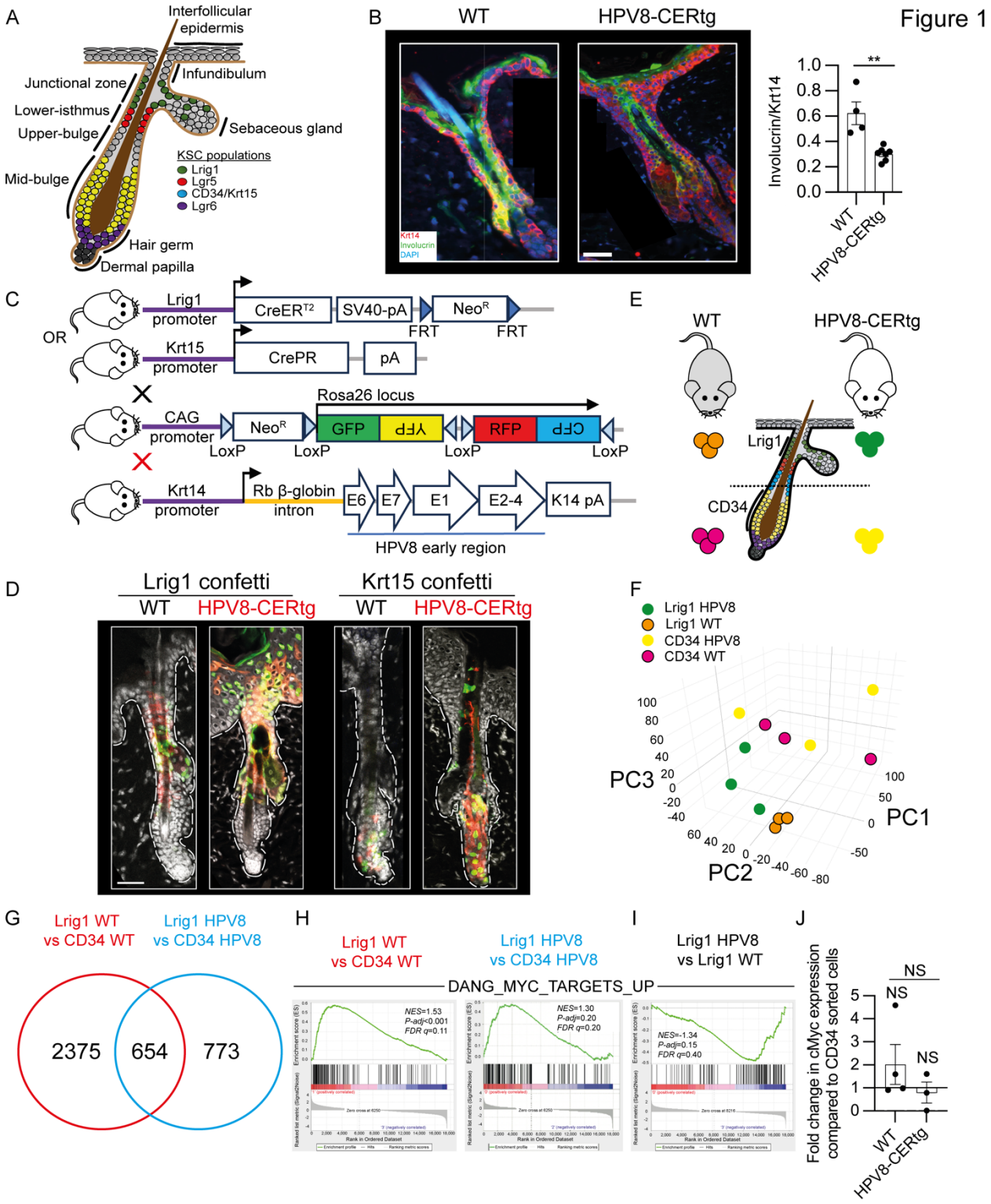

Figure 1. HPV8 induced Lrig1$^+$ hair follicle junctional zone KSC proliferation and expansion. (A) Schematic of hair follicle KSC populations. (B) Immunofluorescent labeling of WT (left) and HPV8-CERtg (right) adult back skin for involucrin (green) and keratin 14 (red), n=11 mice (average of 10 hair follicles/mouse). (C) Schematic summary of four mouse lines that were crossed for lineage tracing. (D) CLSM images of Lrig1 (left) and Keratin 15 (right) promoter-driven confetti reporter expression in progeny of WT (left) and HPV8-CERtg (right) adult back skin. (E) Experimental strategy for flow-sorting Lrig1$^+$ and CD34$^+$ populations for within-mouse comparisons. See also Supplemental Figure 1. (F) PCA of RNA-seq transcriptome analysis of skin KSC populations. (G) Venn diagram showing shared DEGs from Lrig1 vs CD34 comparisons (see Supplemental Table 1). (H) GSEA for c-Myc-regulated genes in DEGs from transcriptomic analysis. (I) GSEA for c-Myc-regulated genes in DEGs from Lrig1 flow sorted HPV8-CERtg vs WT transcriptomic analysis. (J) QPCR of RNA from flow-sorted cell isolated as in (E). All scale bars = 40μm. See also Supplemental Figure 1. Statistical test(s) Figure 1B 2-tailed Student's t-test, Figure 1J one-way ANOVA. ***P*<0.01.

Figure 2

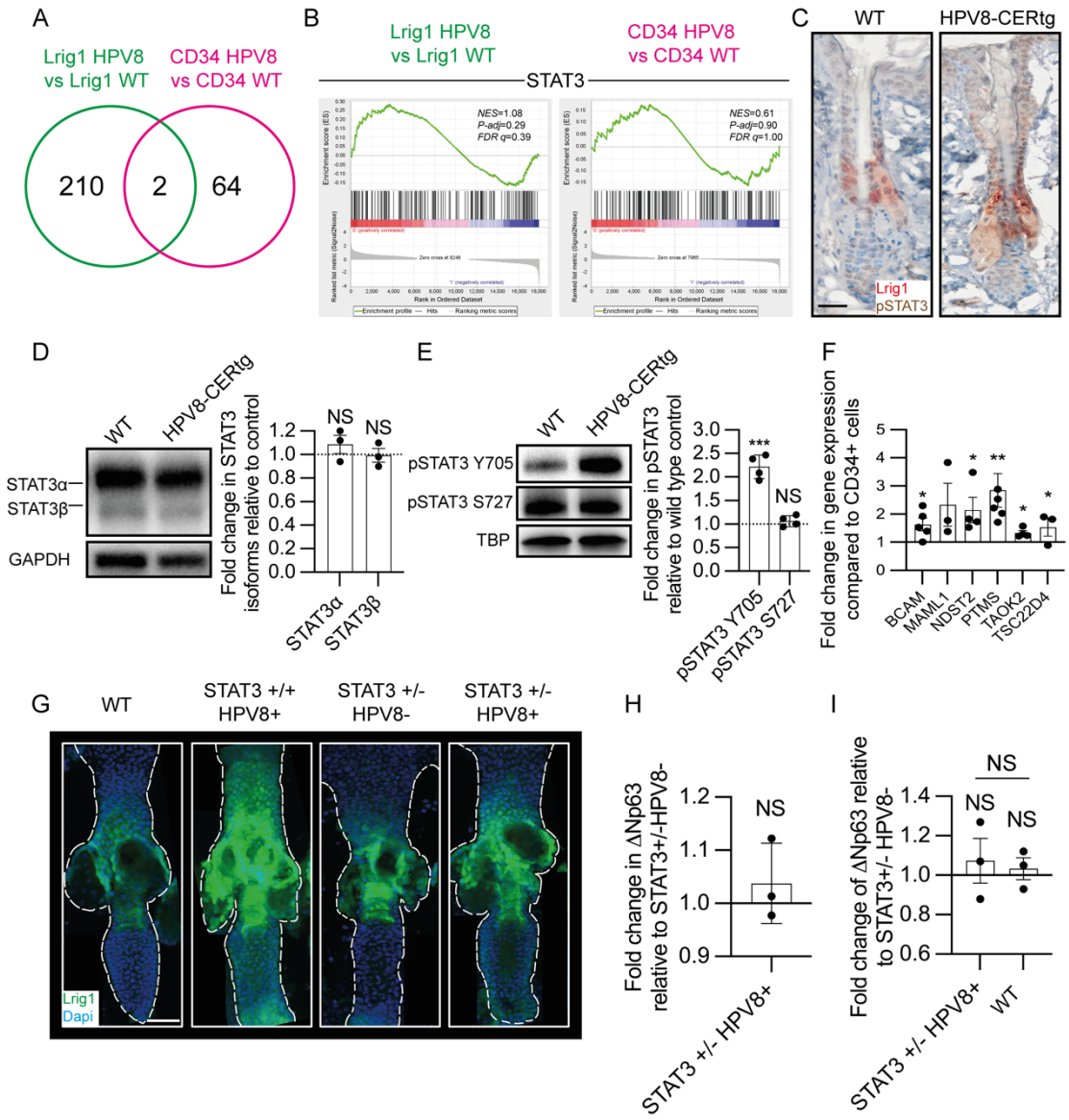

Figure 2. Activated STAT3 regulatory node in HPV8 in Lrig1$^+$ hair follicle junctional zone KSC. (A) Venn diagram showing shared DEGs from HPV8-CERtg vs WT KSC comparisons. (B) GSEA for STAT3-regulated genes in DEGs from transcriptomic analysis. See also Supplemental Figure 2. (C) IHC for pSTAT3 on adult back skin from WT and HPV8-CERtg mice. (D) Immunoblot of total STAT3 (α and β isoforms) in WT and HPV8-CERtg of adult back skin epidermal sheet extracts (n=3). Dotted line is the comparator. (E) Immunoblot of pSTAT3 Y705 and S727 in WT and HPV8-CERtg of adult back skin epidermal sheet nuclear extracts (n=4). Dotted line is the comparator. (F) QPCR of RNA from flow-sorted cell isolates as in (1E) for STAT3 downstream target genes (n≥3). (G) CLSM of whole mount tail skins from WT, HPV8-CERtg, STAT3$^{+/-}$, and STAT3$^{+/-}$ HPV8-CERtg mice for Lrig1 (green) with DAPI (blue). (H) QPCR of RNA from STAT3$^{+/-}$ and STAT3$^{+/-}$ HPV8-CERtg adult back skin epidermal sheets for ΔNp63 (n=3). (I) QPCR of RNA from WT, STAT3$^{+/-}$ and STAT3$^{+/-}$ HPV8-CERtg flow sorted Lrig1$^+$ KSC cell for ΔNp63 (n=3). All scale bars = 40μm. Statistical test(s) Figure 2D, E, F and H 2-tailed Student's t-test, Figure 2I one-way ANOVA. *P<0.05; **P<0.01; ***P<0.001.

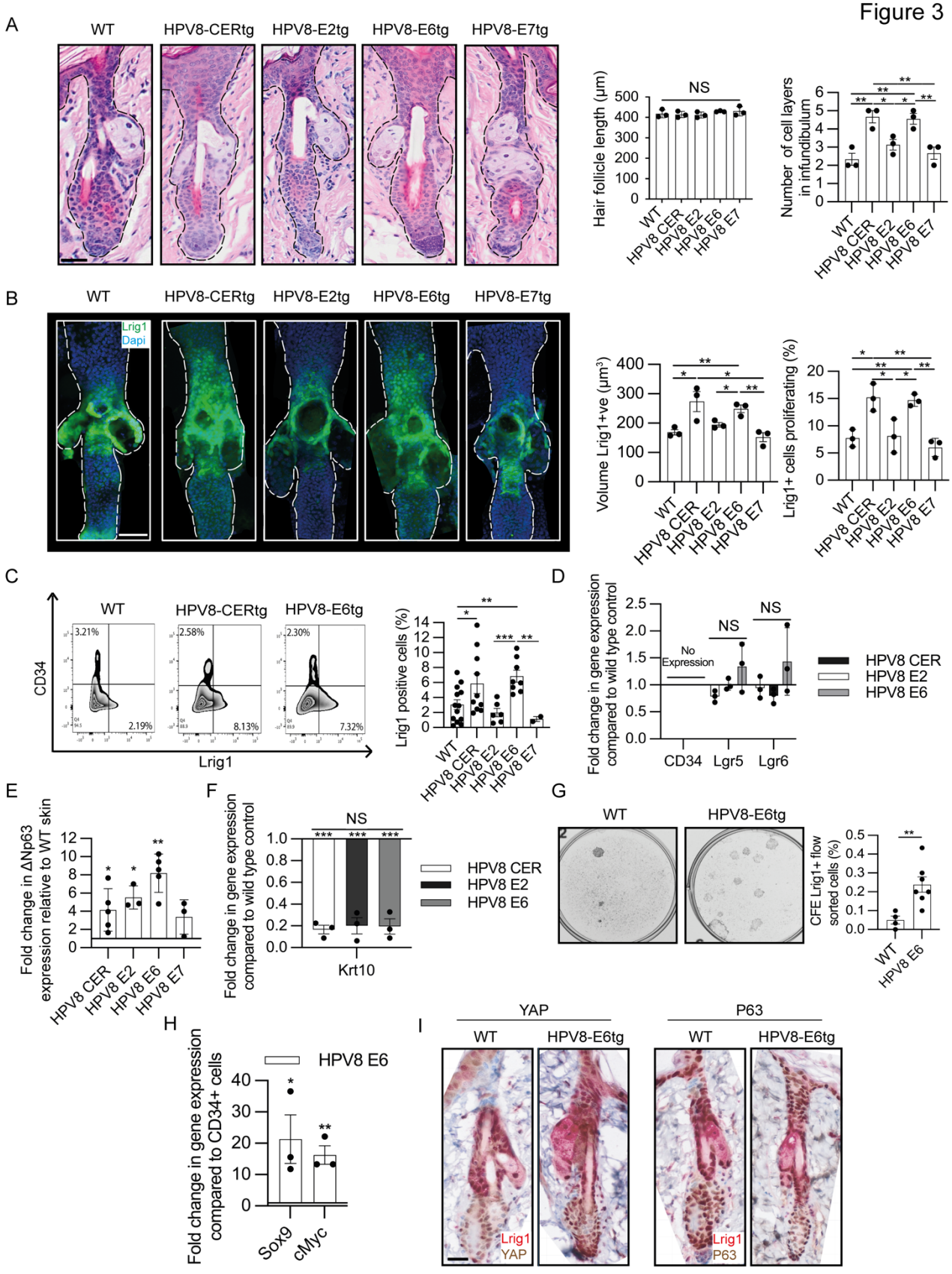

Figure 3. HPV8 E6 drives Lrig1$^+$ hair follicle junctional zone KSC proliferation and expansion. (A) Haematoxylin and Eosin-stained sections from WT, HPV8-CERtg, HPV8-E2tg, HPV8-E6tg, and HPV8-E7tg adult back skin, with quantification of hair follicle length and number of cell layers in the infundibulum (n=3 mice/genotype, average of 20-50 hair follicles/mouse). (B) CLSM of whole mount tail skins as in (A) labeled for Lrig1, with quantification of Lrig1 labeled volume and the number of co-labeled Ki67+ cells (average of 10 hair follicles/mouse). (C) FACS for Lrig1 and CD34 positive populations from back skin cell isolates as in (A) (n=39 total). (D) QPCR of RNA from Lrig1$^+$ flow-sorted cell isolates as in (A) for KSC markers (n=3). (E) QPCR of RNA from Lrig1$^+$ flow-sorted cell isolates as in (A) for ΔNp63 (n=20 total). (F) QPCR of RNA from Lrig1$^+$ flow-sorted cell isolates as in (A) for keratin 10 (n= 3). (G) CFE of 2500 flow-sorted Lrig1$^+$ keratinocytes from WT and HPV8-E6tg adult back skin epidermal sheets (n=11 total). (H) QPCR of RNA from Lrig1$^+$ and CD34$^+$ flow-sorted cell isolates from HPV8-E6tg adult back skin epidermal sheets (n=3). (I) IHC for Lrig1 together with YAP (left) or p63 (right) on WT and HPV8-E6tg adult back skin. All scale bars = 40µm. See also Supplemental Figure 2. Statistical test(s) Figure 3A, B, C, D, E and F one-way ANOVA, Figure 3G and H 2-tailed Student's t-test. *P<0.05; **P<0.01; ***P<0.001.

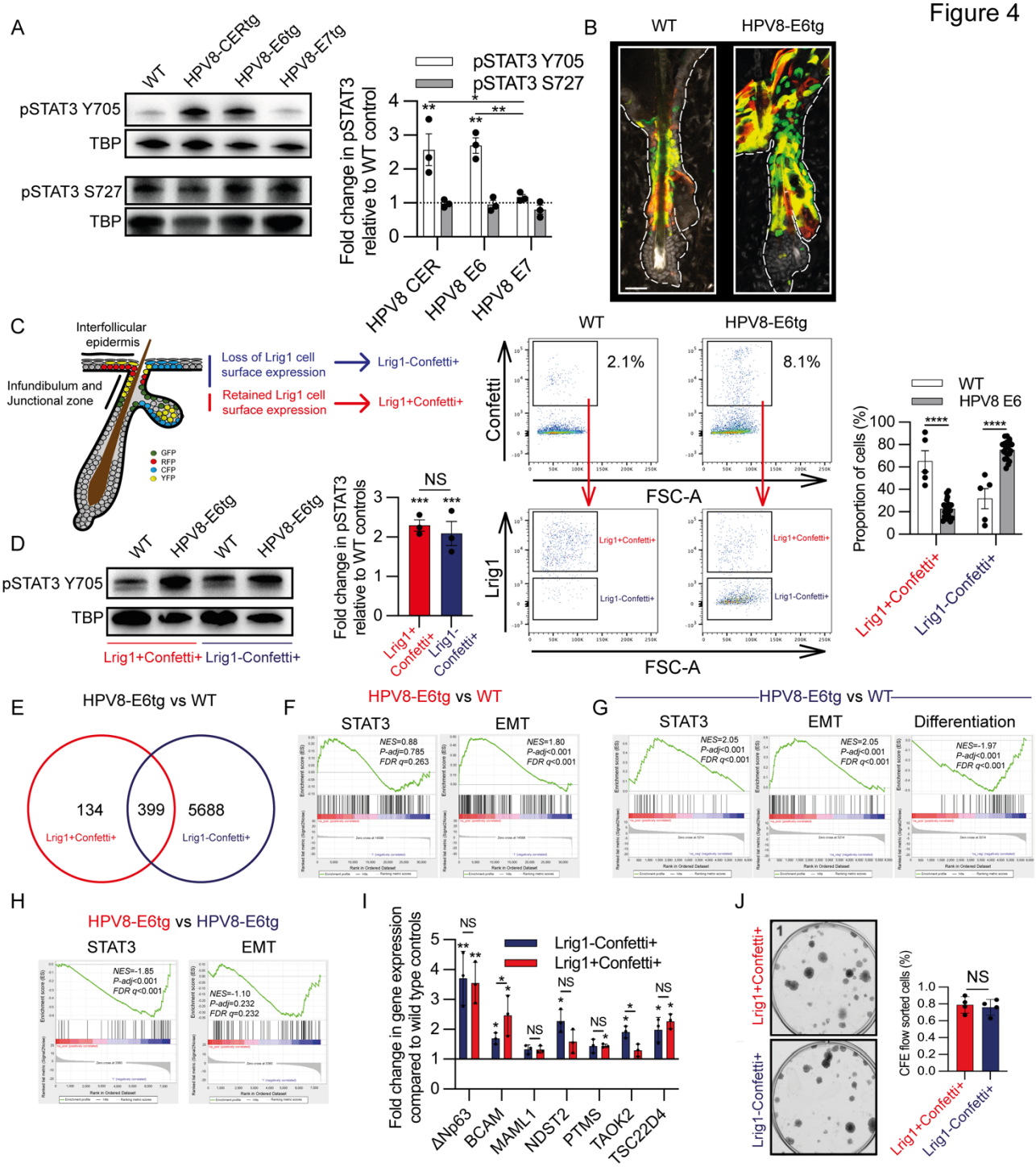

Figure 4. Lrig1$^+$ hair follicle junctional zone KSC progeny retain KSCs. (A) Immunoblot of pSTAT3 Y705 and S727, with TATA-Box binding protein (TBP) control (n=3). (B) CLSM of dorsal back skin for lineage tracing of Lrig1CreER^{T2}:R26RConfetti:WT and Lrig1CreER^{T2}:R26RConfetti:HPV8-E6tg progeny, after 4-weeks post Cre activation. Scale bar = 40μm. (C) Enumerated Lrig1$^+$ confetti$^+$ and their progeny Lrig1$^-$ confetti$^+$ flow-sorted cell populations from Lrig1CreER^{T2}:R26RConfetti:HPV8-E6tg and Lrig1CreER^{T2}:R26RConfetti:WT mice (n=25 total). (D) Immunoblot of Lrig1$^+$ confetti$^+$ and their progeny Lrig1$^-$ confetti$^+$ flow-sorted cell populations (n=3). (E) Venn diagram showing shared DEGs from Confetti HPV8 E6 vs Confetti WT comparisons for Lrig1$^+$ confetti$^+$ and Lrig1$^-$ confetti$^+$ populations (see Supplemental Table 2). (F) GSEA for STAT3- and EMT-associated gene signatures in DEGs from Lrig1$^+$ confetti$^+$ transcriptomic comparison of Confetti HPV8 E6 vs Confetti WT analysis. (G) GSEA for STAT3-, EMT- and differentiation-associated gene signatures in DEGs from Lrig1$^-$ confetti$^+$ transcriptomic comparison of Confetti HPV8 E6 vs Confetti WT analysis. (H) GSEA for STAT3- and EMT-associated gene signatures in DEGs from Confetti HPV8 E6 transcriptomic comparison of Lrig1$^+$ confetti$^+$ and Lrig1$^-$ confetti$^+$ population analysis. See also Figure S3. (I) QPCR of RNA from flow-sorted cell isolates as in (C) for STAT3-regulated genes (n=3). (J) CFE of 2500 flow-sorted Lrig1$^+$ confetti$^+$ and Lrig1$^-$ confetti$^+$ flow-sorted cell populations from Lrig1CreER^{T2}:R26RConfetti:HPV8-E6tg (n=4). See also Supplemental Figure 3. Statistical test(s) Figure 4A, D and I one-way ANOVA, Figure 4C and J 2-tailed Student's t-test. *P<0.05; **P<0.01; ***P<0.001; ****P<0.0001.

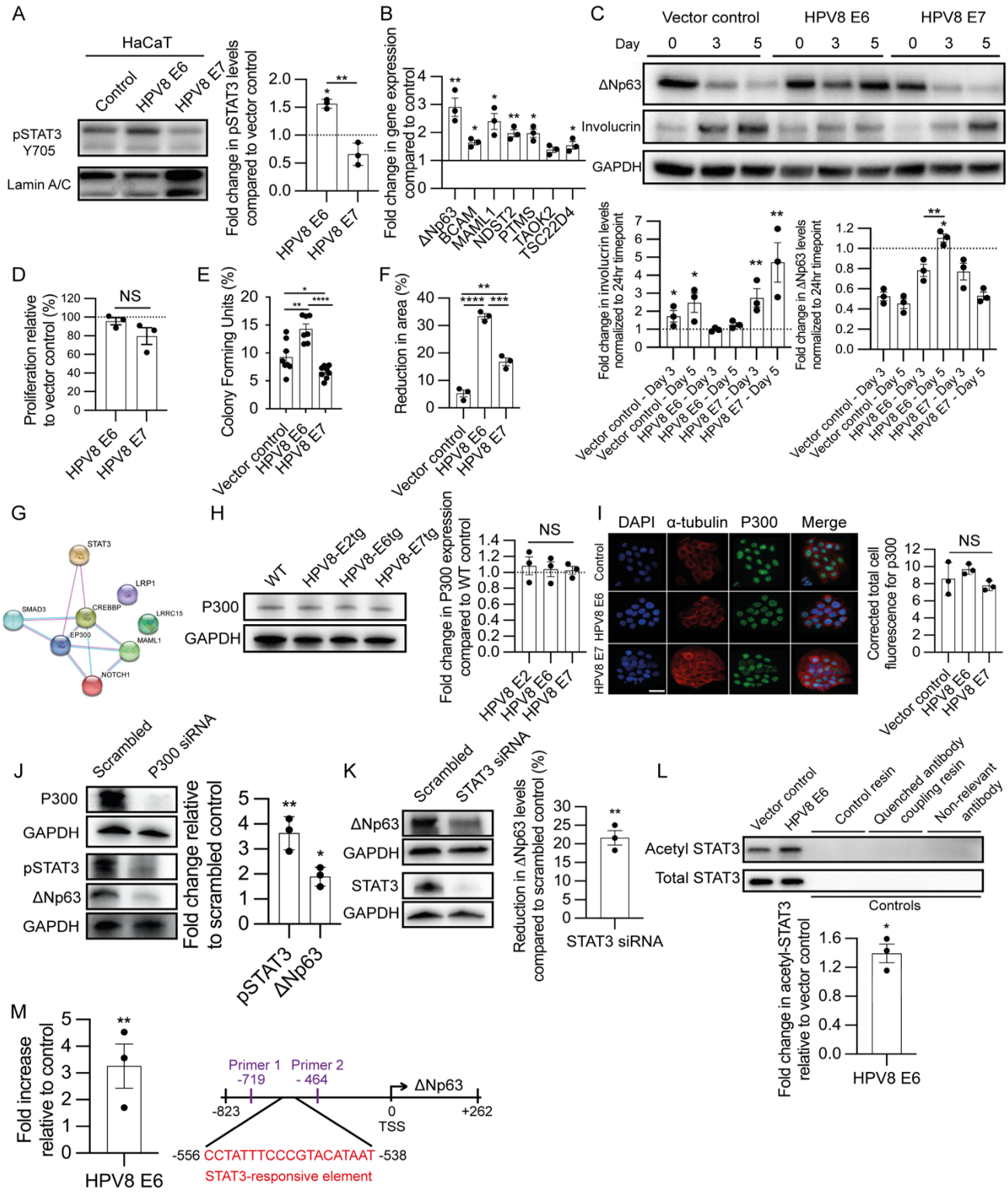

Figure 5. HPV8 E6 P300 interaction activates STAT3. (A) pSTAT3 Y705 immunoblot, with laminin A/C control, of nuclear extracts from transduced HaCaT keratinocytes (n=3). (B) qPCR of RNA from transduced HaCaT keratinocytes for STAT3-regulated genes, with b-actin as control (n=3). (C) Immunoblot of ΔNp63 and involucrin, with GAPDH as control, of transduced HaCaT keratinocytes cultured in high calcium (60 μm) media for 3 and 5 days (n=3). Proliferation (n=3) (D), CFE assay (n=7) (E), and migration (n=3) (F) of transduced HaCaT keratinocytes. (G) String™ analysis demonstrating the interaction of known HPV8 E6 protein binding partners and STAT3. Line colours define interactions as experimentally determined (pink) or from curated database (blue). (H) P300 with GAPDH control immunoblot of WT and HPV8-E2tg, -E6tg and -E7tg mouse keratinocytes (n=3/genotype). (I) P300, a-tubulin and DAPI immunofluorescence labeling of transduced HaCaT keratinocytes (n=3). Scale bar = 40mm. (J) P300, pSTAT3 Y705 and ΔNp63 immunoblot, with GAPDH endogenous control, of HPV8 E6 transduced HaCaT keratinocytes treated with scrambled control and p300 targeting siRNA (n=3). (K) STAT3 and ΔNp63 immunoblot, with GAPDH control, of HPV8 E6 transduced HaCaT keratinocytes treated with scrambled control and STAT3 targeting siRNA (n=3). (L) Immunoblot of STAT3 immunoprecipitated nuclear protein from vector and HPV8 E6 transduced HaCaT keratinocytes probed for acetylated STAT3 and total STAT3 (n=3). (M) qPCR analysis of ΔNp63 primers on STAT3 chromatin immunoprecipitants in HPV8 E6 transduced HaCaT keratinocytes relative to vector (n=3) Schematic of the 5'-flanking region indicating primers sequences relative to STAT3-RE and ΔNp63 TSS. See also Supplemental Figure 4. Statistical test(s) Figures 5A, C, D, E, F, H and I one-way ANOVA, Figure 5B, J, K, L and M 2-tailed Student's t-test. *P<0.05; **P<0.01; ***P<0.001; ****P<0.0001.

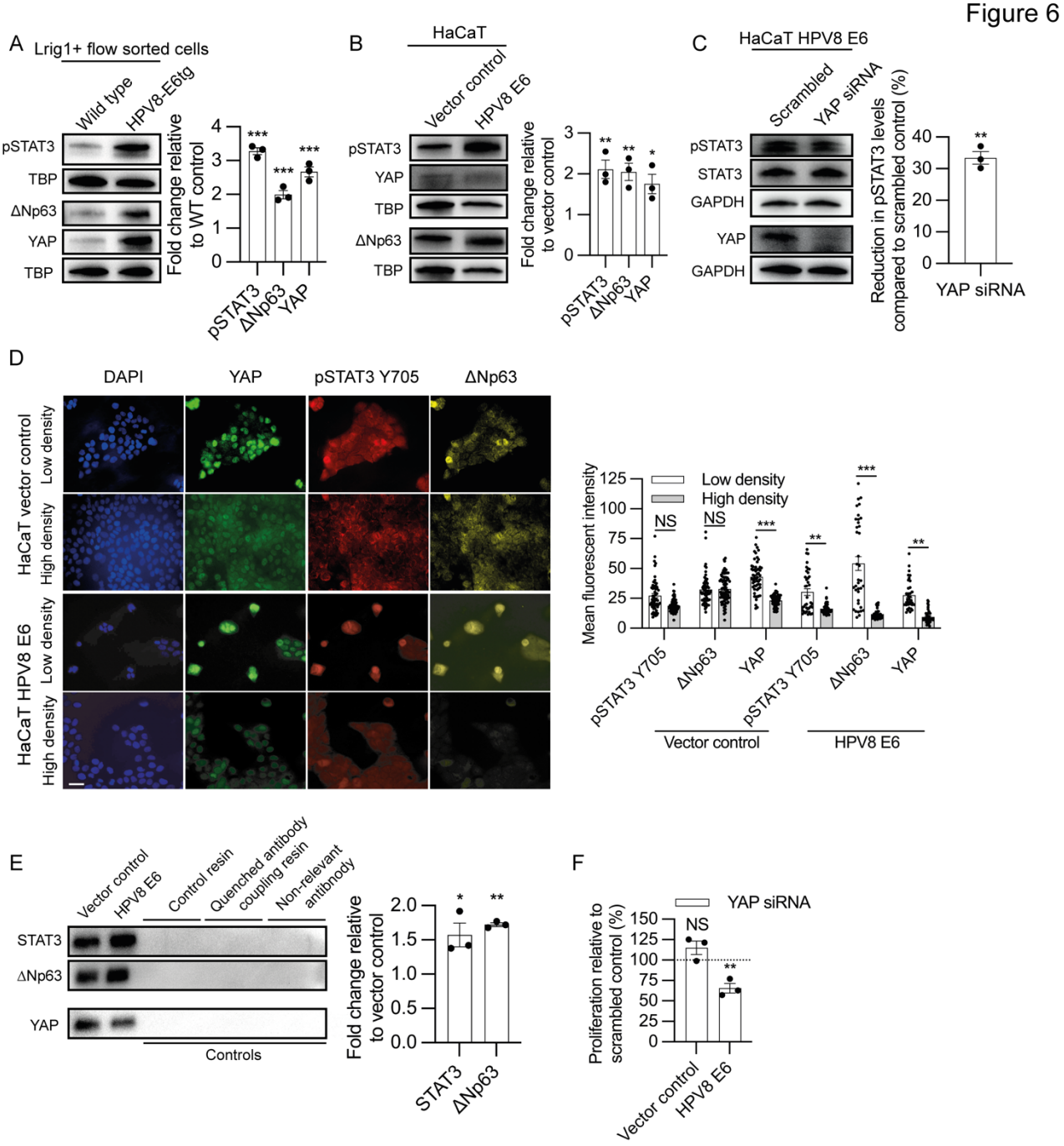

Figure 6. YAP a co-transcription factor for STAT3 and ΔNp63. (A and B) pSTAT3 Y705, ΔNp63 and YAP immunoblot, with TATA-box binding protein endogenous control, of nuclear extracts from Lrig1$^+$ flow-sorted WT and HPV8-E6tg mouse keratinocytes (A) and HPV8 E6 and vector control transduced HaCaT keratinocytes (B) (n=3 per genotype/cell line). (C) pSTAT3 Y705, total STAT3 and YAP immunoblot, with GAPDH endogenous loading control, of HPV8 E6 transduced HaCaT keratinocytes treated with scrambled control and YAP targeting siRNA (n=3). (D) Immunofluorescent labeling of HPV8 E6 and vector control transduced HaCaT keratinocytes cultured at low (~50%) and high (~90%) confluency for YAP (green), pSTAT3 Y705 (red) and ΔNp63 (yellow), with quantification of nuclear mean fluorescent intensity (n=82 cells total quantified over three independent experiments). Scale bar = 40μm. (E) Immunoblot of YAP immunoprecipitated nuclear protein from vector control and HPV8 E6 transduced HaCaT probed for STAT3 and ΔNp63 (n=3). (F) Proliferation of HPV8 E6 and vector control transduced HaCaT keratinocytes assessed by 24 hours of BrdU incorporation following treatment with YAP targeting siRNA (n=3). See also Supplemental Figure 5. Statistical test(s) Figure 6A, B, C, D and E 2-tailed Student's t-test, Figure 6F one-way ANOVA. *P<0.05; **P<0.01; ***P<0.001.

Figure 7

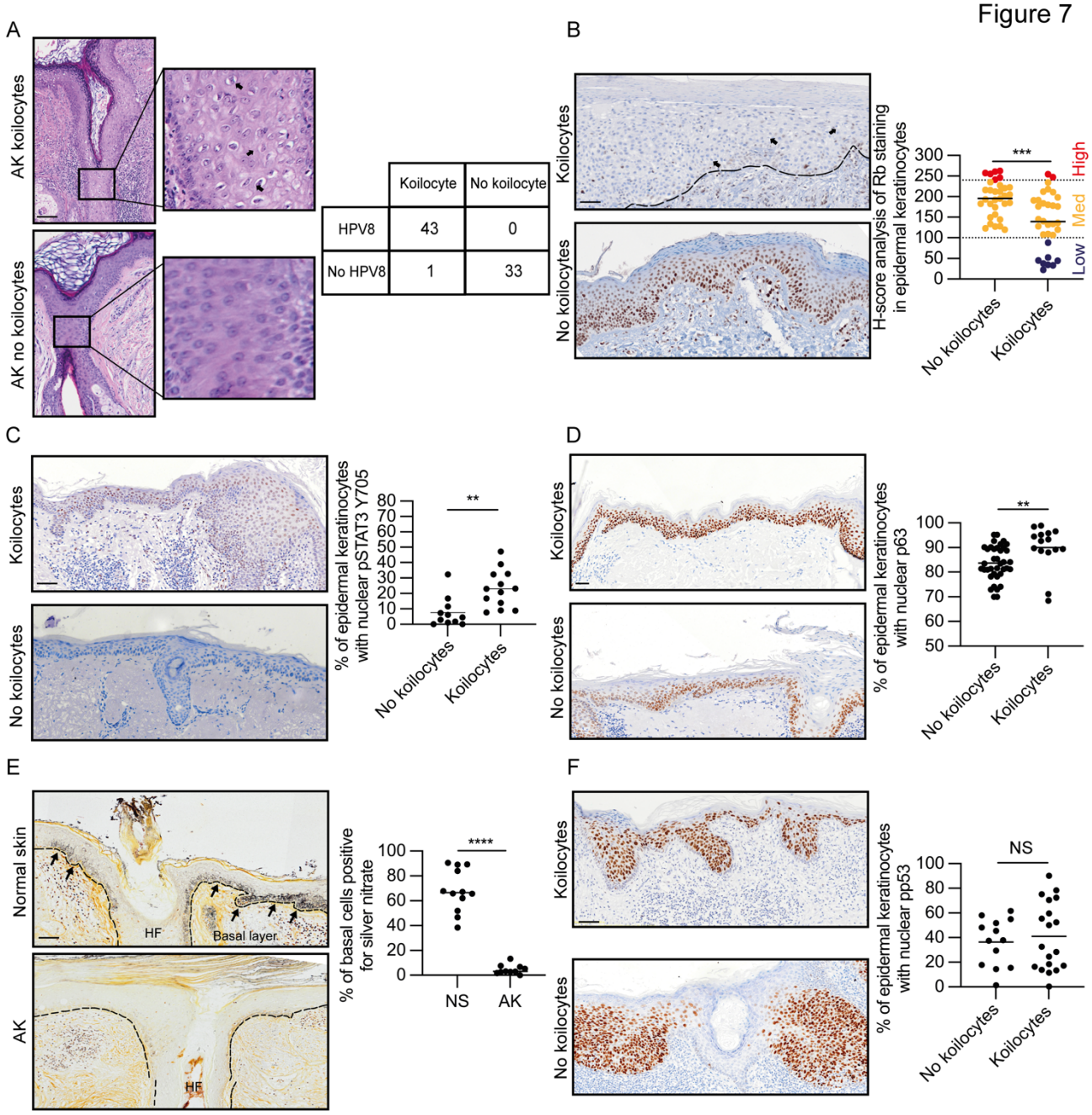

Figure 7. HPV8 reactivation in actinic keratosis with koilocytes. (A) (Left) Haematoxylin and Eosin-stained human AK sections with and without koilocytes. (Right) Presence of koilocytes by HPV8 detection using β-HPV L1 open reading frame PCR-reverse hybridisation assay. See also Supplemental Figure 6A. Arrows indicate the presence of koilocytes. (B-D) IHC of human AK tissue for Rb (n=64), pSTAT3 Y705 (n=24) and p63 (n=53). Arrows indicate the presence of koilocytes. (E) Warthin-Starry stain of human AK tissue (n=24). (F) IHC of human AK tissue for p53 (n=32). All scale bars = 50μm. See also Supplemental Figure 6. Statistical test(s) Figure 7B, C, D, E and F 2-tailed Student's t-test. ***P*<0.01; ****P*<0.001; *****P*<0.0001.

Supplemental Table 1. List of significant differentially expressed genes (adjusted p < 0.05), Related to Figures 1, 2 and Supplemental Figure 1

For each gene, given are Log_2FC. Each tab represents a different comparison.

Supplemental Table 2. List of significant differentially expressed genes (adjusted p < 0.05), Related to Figures 4 and Supplemental Figure 3

For each gene, given are Log_2FC. Each tab represents a different comparison.

Supplemental Table 3. List of activated 'Hallmark', 'Biocarta' and 'Wikipathways' pathways following gene set enrichment analysis on HPV8-E6tg vs WT